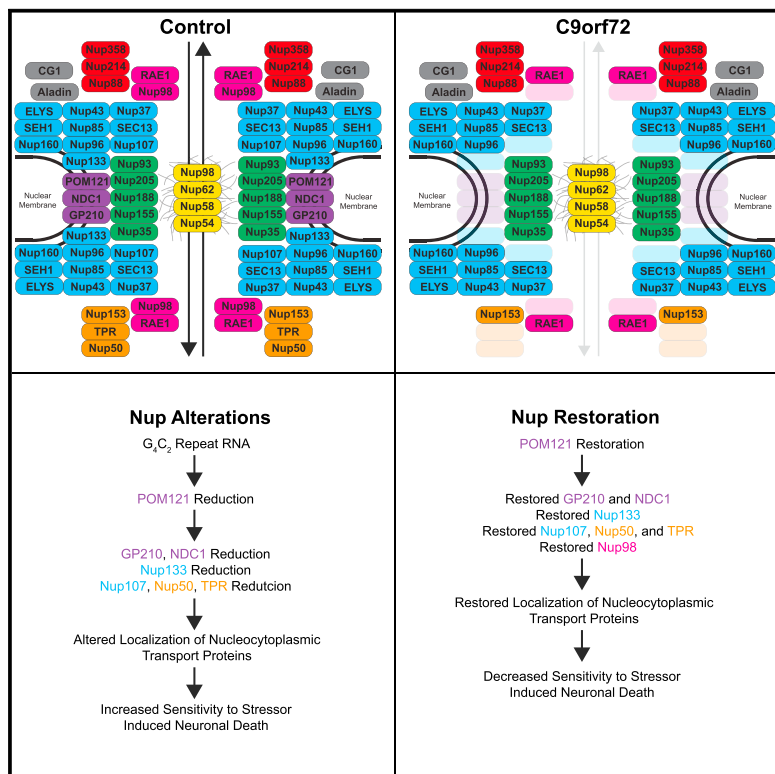


G₄C₂ Repeat RNA Initiates a POM121-Mediated Reduction in Specific Nucleoporins in C9orf72 ALS/FTD

Graphical Abstract



Authors

Alyssa N. Coyne, Benjamin L. Zaepfel, Lindsey Hayes, ..., Clive N. Svendsen, Dhruv Sareen, Jeffrey D. Rothstein

Correspondence

jrothstein@jhmi.edu

In Brief

Coyne et al. demonstrate that G₄C₂ repeat RNA initiates a reduction of POM121 expression within C9orf72 neuronal nuclear pore complexes. Decreased nuclear POM121 affects the expression of seven additional nucleoporins, resulting in altered nuclear pore composition. This combined nucleoporin reduction affects the localization of nucleocytoplastic transport proteins and neuronal survival.

Highlights

- Expression of eight nucleoporins is reduced in human C9orf72 neuronal nuclei
- Reduction in POM121 affects nuclear pore complex composition
- Nucleoporin alterations diminish nucleocytoplastic transport and neuronal survival
- G₄C₂ repeat RNA initiates the pathogenic cascades, leading to decreased nuclear POM121

Article

G₄C₂ Repeat RNA Initiates a POM121-Mediated Reduction in Specific Nucleoporins in C9orf72 ALS/FTD

Alyssa N. Coyne,^{1,2} Benjamin L. Zaepfel,³ Lindsey Hayes,² Boris Fitchman,⁴ Yuval Salzberg,⁴ En-Ching Luo,⁵ Kelly Bowen,¹ Hannah Trost,⁶ Stefan Aigner,⁷ Frank Rigo,⁸ Gene W. Yeo,^{7,9} Amnon Harel,⁴ Clive N. Svendsen,⁶ Dhruv Sareen,⁶ and Jeffrey D. Rothstein^{1,2,10,*}

¹Brain Science Institute, Johns Hopkins University School of Medicine, Baltimore, MD 21205, USA

²Department of Neurology, Johns Hopkins University School of Medicine, Baltimore, MD 21205, USA

³Biochemistry, Cellular, and Molecular Biology Graduate Program, Johns Hopkins University School of Medicine, Baltimore, MD 21205, USA

⁴Azrieli Faculty of Medicine, Bar-Ilan University, Safed 1311502, Israel

⁵Bioengineering Graduate Program, University of California San Diego College of Engineering, La Jolla, CA 92037, USA

⁶The Board of Governors Regenerative Medicine Institute, Cedars-Sinai Medical Center, Los Angeles, CA 90048, USA

⁷Sanford Consortium for Regenerative Medicine, University of California San Diego, La Jolla, CA 92037, USA

⁸Ionis Pharmaceuticals, Carlsbad, CA 92010, USA

⁹Department of Cellular and Molecular Medicine, University of California San Diego, La Jolla, CA 92037, USA

¹⁰Lead Contact

*Correspondence: jrothstein@jhmi.edu

<https://doi.org/10.1016/j.neuron.2020.06.027>

SUMMARY

Through mechanisms that remain poorly defined, defects in nucleocytoplasmic transport and accumulations of specific nuclear-pore-complex-associated proteins have been reported in multiple neurodegenerative diseases, including *C9orf72* Amyotrophic Lateral Sclerosis and Frontotemporal Dementia (ALS/FTD). Using super-resolution structured illumination microscopy, we have explored the mechanism by which nucleoporins are altered in nuclei isolated from *C9orf72* induced pluripotent stem-cell-derived neurons (iPSNs). Of the 23 nucleoporins evaluated, we observed a reduction in a subset of 8, including key components of the nuclear pore complex scaffold and the transmembrane nucleoporin POM121. Reduction in POM121 appears to initiate a decrease in the expression of seven additional nucleoporins, ultimately affecting the localization of Ran GTPase and subsequent cellular toxicity in *C9orf72* iPSNs. Collectively, our data suggest that the expression of expanded *C9orf72* ALS/FTD repeat RNA alone affects nuclear POM121 expression in the initiation of a pathological cascade affecting nucleoporin levels within neuronal nuclei and ultimately downstream neuronal survival.

INTRODUCTION

A GGGGCC (G₄C₂) hexanucleotide repeat expansion (HRE) in intron 1 of the *C9orf72* gene is causative of familial and sporadic forms of the motor neuron disease amyotrophic lateral sclerosis (ALS) and the second most common form of dementia, frontotemporal dementia (FTD) (DeJesus-Hernandez et al., 2011; Renton et al., 2011). The HRE is bidirectionally transcribed to form sense (G₄C₂) and antisense (G₂C₄) RNA species that pathologically accumulate into nuclear RNA foci. Repeat associated non-ATG translation (RANT) of G₄C₂ and G₂C₄ RNA produces five dipeptide repeat (DPR) proteins [poly(GA), poly(GP), poly(GR), poly(PR), and poly(PA)]. Together, these RNA species and DPR proteins are thought to contribute to disease through gain-of-toxicity mechanisms. In addition, the *C9orf72* HRE may also lead to haploinsufficiency of the C9ORF72 protein, resulting

in a mild cellular, but not clinical, loss-of-function phenotype (Gitler and Tsuji, 2016; Taylor et al., 2016). Recently, alterations in an essential cellular process, nucleocytoplasmic transport (NCT), have been identified in models of *C9orf72* ALS/FTD (Freibam et al., 2015; Jovićić et al., 2015; Zhang et al., 2015). However, the molecular mechanisms underlying these disruptions and the normal biology governing NCT in human neurons remain largely unknown.

The mammalian nuclear pore complex (NPC) is a ~120-MDa protein complex consisting of multiple copies of approximately 30 nucleoporins (Nups) that collectively function to maintain NCT, genome organization, and gene expression. These Nups are found within modular subcomplexes that form the major architectural units of the NPC, including the outer and inner ring complexes that form the core NPC scaffold. This scaffold is anchored to the nuclear envelope by transmembrane Nups.

Ultimately, this structure anchors the cytoplasmic filaments, nuclear basket, and central transport channel. The central channel is comprised of intrinsically disordered proteins containing multiple FG-repeat motifs. They establish a size-selective diffusion barrier and transport channel for nuclear transport receptors (NTRs) and their bound cargo (Beck and Hurt, 2017; Li et al., 2016; Lin and Huelz, 2019; Raices and D'Angelo, 2012). Additionally, a subset of Nups can also function outside the NPC in regulating gene transcription (Pascual-Garcia and Capelson, 2019).

Although small (<5 nm) macromolecules can passively diffuse through the NPC (Popken et al., 2015; Timney et al., 2016), the nuclear transport of signal-bearing macromolecules is mediated by NTRs (also called karyopherins, importins, and exportins). NTRs recognize import and export signals and transport cargo through the NPC by binding to FG-repeat sequences. The energy to fuel multiple transport cycles is provided by Ran GTPase that binds to NTRs in its GTP-bound form to destabilize import complexes and stabilize export complexes. As a result, in order for bidirectional nuclear transport to occur, a chromatin-bound RanGEF (RCC1) ensures that RanGTP is maintained at high levels within the nucleus and that RanGAP drives GTP hydrolysis in the cytoplasm (Melchior, 2001; Raices and D'Angelo, 2012). The relative steady-state localization of Ran between the nucleus and cytoplasm has previously been used as a metric for global alterations to NCT and cellular function in neurodegenerative disease models (Eftekharzadeh et al., 2018; Grima et al., 2017; Zhang et al., 2015).

Scaffold Nups are extremely long lived in non-dividing cells, including neurons, with many having half-lives measured in months to years. As a result, alterations in NPCs and NCT have been reported during aging (D'Angelo et al., 2009; Hetzer, 2010; Savas et al., 2012; Toyama et al., 2013). In age-related neurodegenerative diseases, such as ALS, Huntington disease (HD), and Alzheimer disease (AD), disruptions in NCT appear to be exacerbated over time (Chou et al., 2018; Eftekharzadeh et al., 2018; Freibaum et al., 2015; Gasset-Rosa et al., 2017; Grima et al., 2017; Jovićić et al., 2015; Zhang et al., 2015). In addition, specific Nups have been reported as modifiers of C9orf72-mediated toxicity in the *Drosophila* eye (Freibaum et al., 2015). Furthermore, mislocalization of the NPC-associated protein RanGAP1 and Nups has been reported in postmortem human tissue and multiple mouse models based on overexpression of the C9orf72 HRE or individual DPRs (Chew et al., 2019; Zhang et al., 2015, 2016, 2018, 2019b). Collectively, these studies suggest that altered NCT is a primary pathological feature of ALS and FTD. To mechanistically understand how alterations to the NPC and NCT contribute to disease pathogenesis, a comprehensive evaluation of the precise deficits in the context of endogenous C9orf72 HRE expression is necessary.

Here, using an induced pluripotent stem cell (iPSC)-derived neuron (iPSN) model of C9orf72 ALS and super-resolution structured illumination microscopy (SIM), we show that the expression of a specific subset of eight Nups is decreased in human C9orf72 neuronal nuclei and NPCs. Mechanistically, genetic manipulation of candidate Nups reveals that the transmembrane Nup POM121 plays an integral role in maintaining the nuclear levels of these eight NPC components in iPSNs. Loss of

POM121 in C9orf72 ALS/FTD is not mediated by DPRs or a loss of the C9ORF72 protein but occurs in the presence of pathologic G₄C₂ repeat RNA. These data provide direct evidence that pathologic repeat RNA initiates early disruptions to the NPC in C9orf72-mediated disease. Ultimately, alterations in NPC-associated POM121 subsequently affect the nuclear and NPC-associated repertoire of an additional seven Nups, and collectively, these alterations affect the distribution of Ran GTPase and cellular toxicity.

RESULTS

Characterization of C9orf72 Pathology in an Accelerated iPSC-Derived Spinal Neuron Differentiation Protocol

Although the use of postmortem human tissue is valuable for the identification of pathological hallmarks of disease, the study of neurodegenerative diseases using iPSCs provides an unparalleled opportunity to identify underlying molecular mechanisms of disease pathogenesis. Neurons derived from human iPSCs maintain endogenous expression of disease-associated genes and proteins rather than relying on overexpression models. However, many previous iPSC differentiation protocols take months to generate spinal neurons, leading to increased differentiation and batch variability (Sances et al., 2016; Zhang et al., 2019a). To model C9orf72 ALS with iPSCs, spinal neurons were differentiated using the direct induced motor neuron (diMN) protocol (Figure S1A). With this protocol, terminal differentiation and neuronal maturation begin at day 12 of differentiation with the addition of specific neuronal maturation growth factors (see STAR Methods; Figure S1A). Ultimately, a reproducible population of spinal neurons is generated by day 18 of differentiation, of which about 30% are Islet-1-positive lower motor neurons (Figures S1A and SB). Importantly, C9orf72 ALS/FTD clinically and pathologically affect multiple different populations of spinal and cortical neurons across two clinically distinct but genetically overlapping neurodegenerative diseases (Cook and Petrucci, 2019; Ferrari et al., 2011). Given that more than just Islet-1-positive lower motor neurons are affected in disease, the analysis of all neurons within iPSC-derived spinal neuron cultures is essential for a comprehensive understanding of pathogenic mechanisms. As a result, we began by evaluating C9orf72 pathology in these mixed iPSN cultures. Similar to our previous publications showing iPSNs produce G₄C₂ repeat RNA that can infrequently accumulate into RNA foci (Donnelly et al., 2013), qRT-PCR experiments reveal an age-dependent increase in both G₄C₂ and G₂C₄ repeat RNA from day 18 to day 32 of differentiation (Figure S1C). Conversely, Poly(GP) DPR levels, as detected by immunoassay, remain constant over time for each individual iPSC line tested (Figure S1D), consistent with our previous studies in human cerebrospinal fluid (CSF) showing variability in Poly(GP) levels among individual patients (Gendron et al., 2017). Furthermore, we find a slight reduction in C9orf72 RNA levels (Figure S1E) and no change in C9ORF72 protein (lower band as determined by western blot on C9orf72^{-/-} iPSC line; data not shown; Figures S1F and S1G) at day 32 of differentiation. Taken together, these data suggest that although our iPSN model of C9orf72 ALS recapitulates pathologic repeat

RNA and DPR production, it does not result in haploinsufficiency of C9ORF72, consistent with variability in C9ORF72 protein levels seen in actual patients (Sareen et al., 2013; Waite et al., 2014).

A major pathologic hallmark of most ALS and FTD cases, including *C9orf72*, includes the cytoplasmic mislocalization and accompanying accumulation of the normally nuclear RNA binding protein TDP-43 in a subset of neurons at autopsy (Ling et al., 2013). Using immunostaining and confocal imaging, we show that TDP-43 does not mislocalize to the cytoplasm of *C9orf72* iPSNs compared to controls (Figure S1H and S1) at day 32 of differentiation. In agreement with human biopsy and autopsy studies (Vatsavayai et al., 2016), this finding suggests that TDP-43 mislocalization may be a much later event in ALS pathogenesis. In contrast, although we see no overt difference in cell death at baseline, *C9orf72* iPSNs are susceptible to glutamate-induced excitotoxicity (Figure S1J), similar to our previous reports using a much longer spinal neuron differentiation protocol (Zhang et al., 2015).

Specific Nups Are Altered in *C9orf72* iPSN Nuclei in an Age-Dependent Manner

Previous reports have pathologically characterized cytoplasmic accumulations of a small number of Nups in artificial overexpression model systems and postmortem patient tissue (Chew et al., 2019; Zhang et al., 2015, 2016, 2018, 2019b). However, none of these studies have truly evaluated the expression of Nups in actual nuclei and NPCs, an analysis critical for the understanding of *C9orf72* HRE-mediated disease pathogenesis.

To examine the nuclear levels of 23 individual human Nups in NeuN-positive nuclei isolated from iPSNs, we used super-resolution SIM. SIM provides an estimated lateral imaging resolution of 100 nm that, unlike standard light microscopy, is sufficient to resolve individual NPCs (Lin and Hoelz, 2019; Maglione and Sigrist, 2013; Schermelleh et al., 2008). However, as human NPCs themselves are ~100 nm in diameter (Lin and Hoelz, 2019), SIM cannot resolve individual Nup molecules within the NPC octet structure. Nonetheless, SIM is routinely used with conventional immunofluorescent staining protocols and specific anti-Nup antibodies to quantify NPC number by counting resolvable “spots” and their intensity on the nuclear envelope (Maglione and Sigrist, 2013; Schermelleh et al., 2008; Thevathasan et al., 2019).

Following SIM, an automated image analysis pipeline was used to determine the number of Nup spots per nucleus. For most of the immunostained Nups, this approach was successful. However, there were a few anti-Nup antibodies that did not produce sufficient signal-to-noise ratios for individual spots to be confidently quantified. In cases in which individual spots could not be resolved, we calculated the percent of the total nucleus volume occupied by the anti-Nup signal (see STAR Methods for additional details). In addition to variable signal-to-noise ratios among individual Nups, we observed that there was variability in the number of spots detected and level of fluorescence among spots for individual Nups (Figures 1A–1C). Although this finding suggests that there may be a different number of Nup molecules per individual NPCs, we note that differential antibody affinities do not allow for a comparison of absolute Nup spot or

volume numbers among each of the 23 Nups evaluated. Thus, all analyses were conducted on an individual Nup basis comparing *C9orf72* to controls. Using this approach, we reproducibly found that 8 of the 23 Nups examined, including the nuclear basket Nups Nup50 and TPR; the central channel Nup Nup98; all three transmembrane Nups GP210, NDC1, and POM121; and the Y complex outer ring Nups Nup107 and Nup133, are significantly reduced in *C9orf72* iPSN nuclei at day 32 but not day 18 when compared to controls at the respective time points (Figure 1). These data highlight the age dependence of specific Nup alterations in the maturation of pathogenic cascades in *C9orf72* ALS.

Interestingly, although individual Nups are localized in close proximity, we rarely observe colocalization between two Nups within the pairings we evaluated (Figure S2). Moreover, in single Z slices from our SIM analyses, we observe areas within iPSN nuclei that contain only one of the Nups in our double immunolabeling experiments (Figure S2), consistent with previous reports of Nup heterogeneity within NPCs in a single nucleus in non-neuronal cellular systems (Kinoshita et al., 2012; Rajoo et al., 2018; Toyama et al., 2018). Nonetheless, in *C9orf72* iPSN nuclei, we observe a reduction in multiple Nups within each neuronal nucleus (Figure S3).

When available, a second antibody targeting an alternate region of Nup proteins was used to verify Nup reduction by SIM. For example, antibodies that recognize both the C (Figures 1A and 1E) and N termini of POM121 (Figures S4A and S4B) revealed a similar reduction in POM121 at day 32 of differentiation. Importantly, we observe a reduction of nuclear POM121 in Islet-1-positive lower motor neurons at day 32 but not at day 18 (Figures S4C and S4D) and in spinal neurons derived using a previously described iPSN differentiation protocol (Donnelly et al., 2013; Zhang et al., 2015; Figures S4E and S4F). Together, these data suggest that our observed alterations in specific Nups are reproducible in multiple neuronal subtypes affected in ALS pathogenesis and across multiple differentiation protocols.

Although isolated nuclei preparations provide for more accurate reconstruction and increased resolution of Nup immunostaining, we observe a similar decrease in POM121, Nup133, and Nup50 nuclear intensity by using standard confocal microscopy in intact iPSNs (Figures S5A–S5D), suggesting that our results are not an artifact of SIM or nuclei isolation. Furthermore, we do not observe mislocalization of POM121, Nup133, or Nup50 from the nucleus to the cytoplasm in intact iPSNs (Figures S5A–S5C). Moreover, we performed additional validation with western blots that quantitatively confirm a decrease in total POM121, Nup133, and Nup50 proteins in isolated nuclei from *C9orf72* iPSNs (Figures S5E and S5F). A reduction in the Nup protein is not a result of decreased steady-state mRNA levels (Figure S5G), altered mRNA stability as measured by actinomycin D chase (Figures S6A–S6J), or decreased association with polyribosomes (Figures S6K–S6T). In fact, for some Nups, the association of their mRNA with actively translating polyribosome fractions is increased in *C9orf72* iPSNs (Figures S6K–S6T) despite the reduced protein expression observed by multiple experimental methodologies. Collectively, these data suggest that nuclear levels of specific Nups are decreased at the level of protein expression and/or stability in *C9orf72* iPSN nuclei.

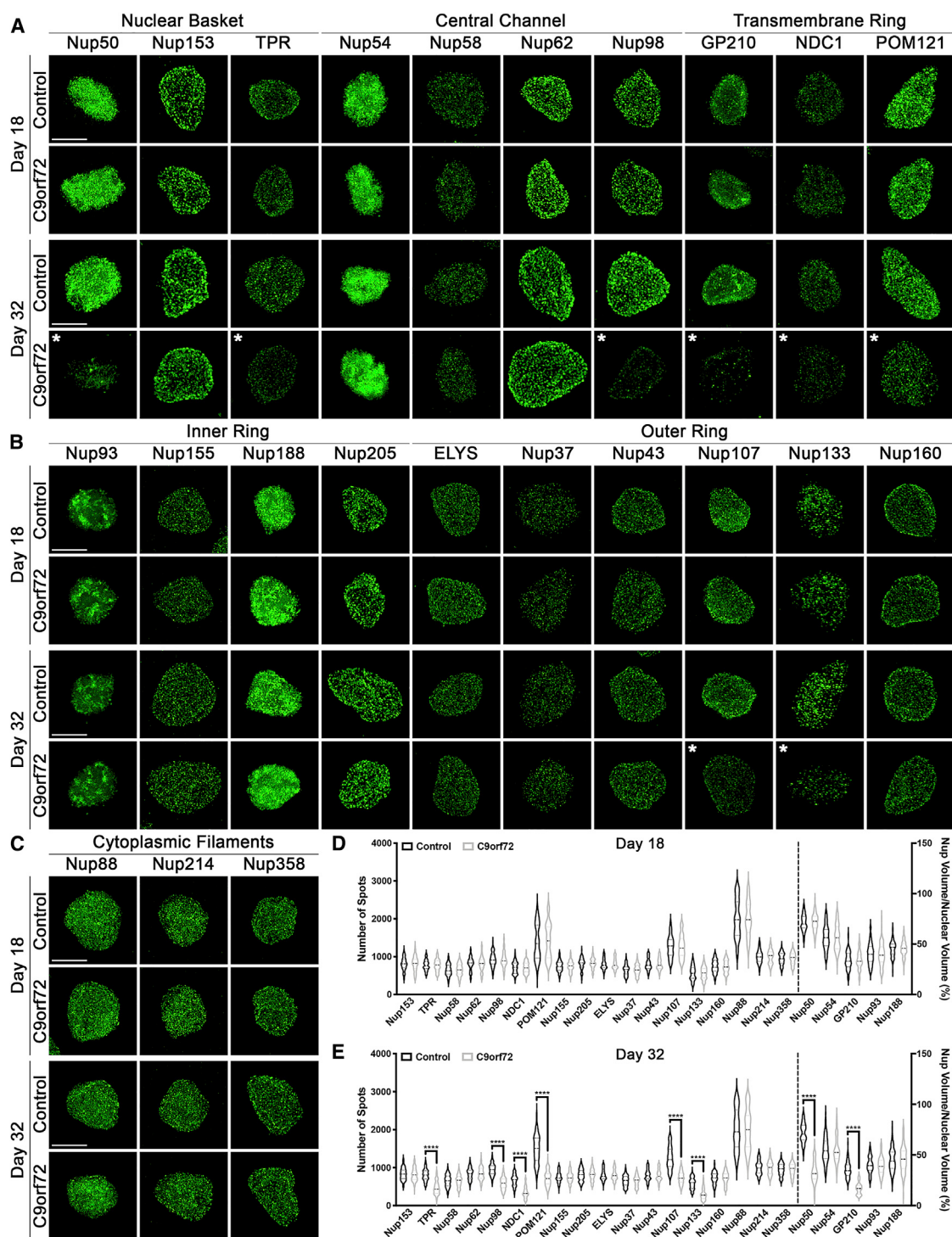


Figure 1. Specific Nucleoporins Are Altered in Nuclei from C9orf72 iPSCs

(A–C) Maximum intensity projections from SIM imaging of Nups in nuclei isolated from control and C9orf72 iPSCs. Genotypes and time points are indicated on left; antibodies indicated on top.

(D–E) Quantification of Nup spots and volume. Time points are indicated on top. n = 8 control and 8 C9orf72 iPSC lines (including 1 isogenic pair), 50 NeuN+ nuclei per line/time point. Two-way ANOVA with Tukey multiple comparison test was used to calculate statistical significance. ***p < 0.0001. Scale bar, 5 μm. * indicates significantly altered Nups.

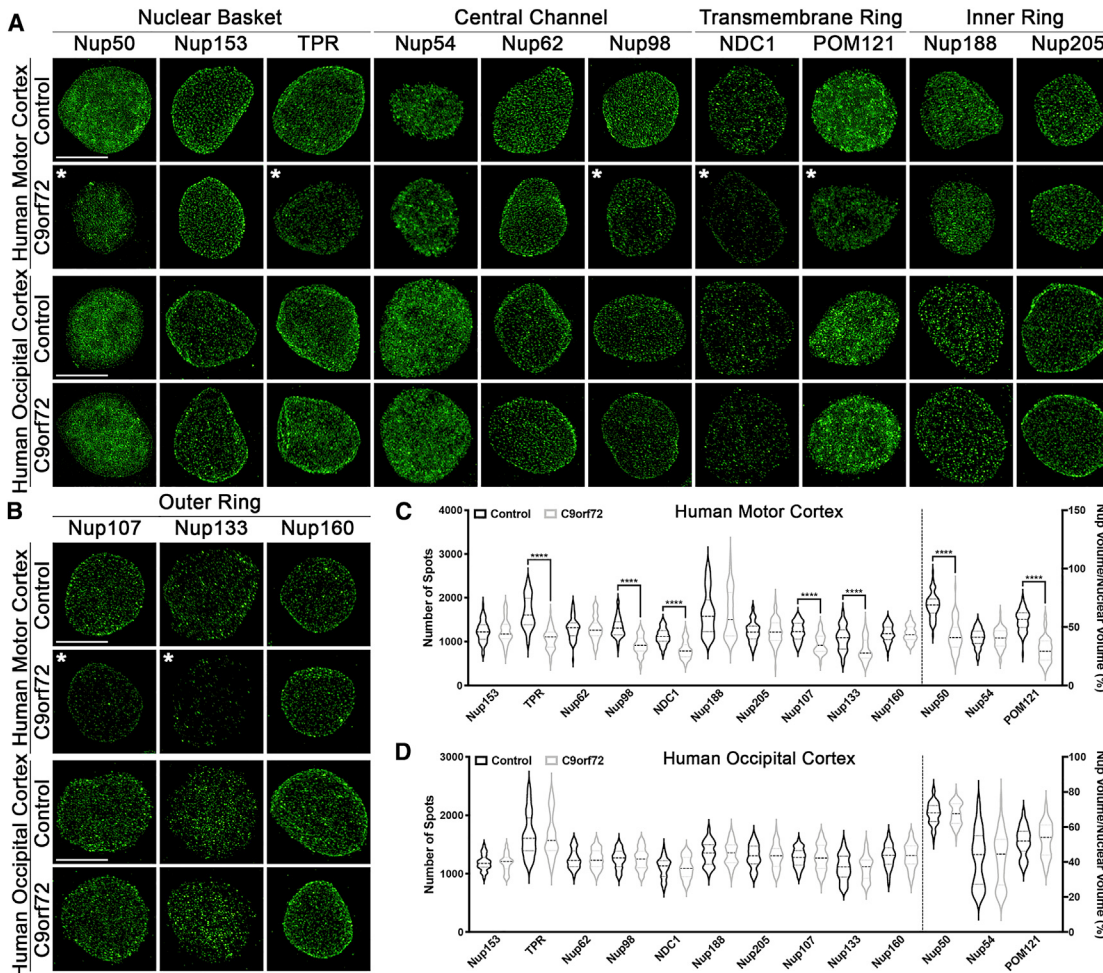


Figure 2. Specific Nucleoporins Are Altered in Nuclei from C9orf72 Patient Motor Cortex

(A and B) Maximum intensity projections from SIM imaging of Nups in nuclei isolated from postmortem human brain tissue. Genotypes and brain regions are indicated on left; antibodies are indicated on top.

(C and D) Quantification of Nup spots and volume. Brain regions are indicated on top. n = 3 control and 3 C9orf72 cases, 50 NeuN+ nuclei per case. Two-way ANOVA with Tukey multiple comparison test was used to calculate statistical significance. ***p < 0.0001. Scale bar, 5 μm. * indicates significantly altered Nups.

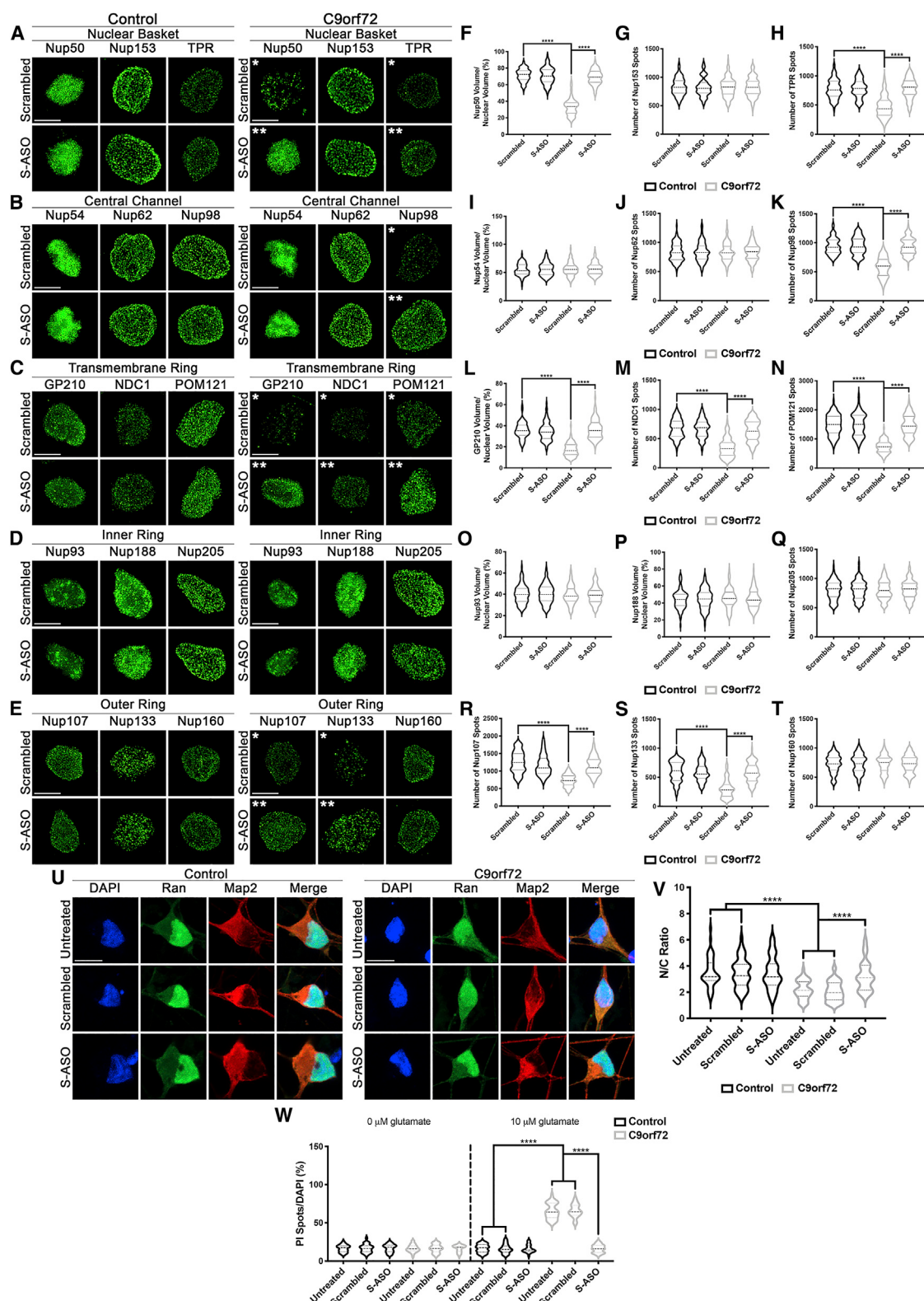
without corresponding cytoplasmic mislocalization or accumulation. Although reduced POM121 in C9orf72 iPSN nuclei is a reproducible and robust pathology across multiple iPSN lines, we note that there is a variable decrease in POM121 among individual nuclei (Figure S7), in accordance with our quantification represented by violin plots. In spite of this variable reduction in eight specific Nups from the nucleus, we do not find alterations in the overall number or distribution of FG-repeat-containing Nups based on immunostaining with a general antibody (mAb414; 414) that recognizes four FG-repeat-containing Nups: Nup153, Nup62, Nup214, and Nup358/RanBP2 (Figures S8A–S8C).

To globally evaluate NPC structure and distribution in control and C9orf72 iPSN nuclear envelopes at high resolution, we used direct surface imaging by field emission scanning electron microscopy (SEM). Here, we found that the overall number and distribution of NPCs is unchanged in C9orf72 iPSN nuclei (Figure S8D). Furthermore, higher magnification imaging

focusing on individual NPCs shows no overt change in NPC architecture in C9orf72 iPSN nuclei (Figure S8D). Together, these data suggest that individual Nup molecules may be reduced from the nuclear envelope, presumably from pore octamers, without an overall loss of NPCs.

C9orf72 iPSN Nuclei Are Not Leaky

Given our previous report that active NCT is disrupted in C9orf72 iPSNs (Zhang et al., 2015) and our data that eight Nups are decreased in C9orf72 iPSN nuclei without overall effects on NPC distribution and structure (Figure 1; Figure S8D), we next wanted to determine if C9orf72 iPSN nuclei were passively leaky. Normally, some macromolecules can passively diffuse through the NPC in a manner dependent on their size (Popken et al., 2015; Timney et al., 2016). Accordingly, fluorescent dextrans of various sizes have been used to evaluate the passive permeability of NPCs (Zhu et al., 2016). Confocal imaging of digitonin-permeabilized iPSNs revealed that C9orf72 nuclei are not



(legend on next page)

passively leaky compared to controls (Figure S9), suggesting that the overall passive permeability barrier of the NPC is intact despite the nuclear reduction in eight specific Nups in C9orf72 iPSNs.

Nucleoporin Alterations in Postmortem C9orf72 Patient Motor Cortex and Thoracic Spinal Cord Are Identical to Those in C9orf72 iPSNs

To determine whether our observed Nup pathology in C9orf72 iPSNs was reflective of real changes that occur in human patients, we next examined isolated nuclei from postmortem motor and occipital cortex from non-neurologic control and C9orf72 patients by SIM. Of the 13 Nups analyzed, Nup50, TPR, Nup98, NDC1, POM121, Nup107, and Nup133 but not Nup153, Nup54, Nup62, Nup93, Nup188, Nup205, or Nup160 are decreased in NeuN-positive nuclei from the C9orf72 patient motor cortex (Figures 2A–2C) but not occipital cortex (Figures 2A, 2B, and 2D), a brain region unaffected in ALS. Similar to our results in the postmortem motor cortex, the nuclear levels of six Nups (Nup50, TPR, NDC1, POM121, Nup107, and Nup133) are reduced in NeuN-positive nuclei isolated from C9orf72 patient thoracic spinal cord compared to controls (Figure S10). Together, these data in patient tissue mimic our results in iPSNs. Notably, staining of postmortem paraffin-embedded motor cortex tissue sections with an antibody recognizing the C terminus of POM121 also shows a decrease in nuclear POM121 intensity (Figure S11), albeit without the resolution provided by SIM. Collectively, these data suggest that our iPSN model recapitulates human disease pathogenesis, identifies specific Nup alterations as a possible initiating pathologic event in C9orf72 ALS, and highlights the use of our iPSN model as a tool for studying the disease mechanisms underlying alterations in individual NPC components.

Reversibility of NPC Injury: Treatment with C9orf72 Sense-Repeat-Targeting ASO Mitigates Alterations in Specific Nups and Cellular Localization of Ran GTPase

Following validation that antisense oligonucleotides (ASOs) targeting the intron upstream of the G₄C₂ repeat (sense strand) could alleviate G₄C₂ pathology in our accelerated iPSN system (Figure S12) in a manner similar to our previous reports (Gendron et al., 2017), we next investigated whether ASO treatment of iPSNs can mitigate alterations in Nup levels within the nucleus. Compared to the scrambled control ASO, 3-week sense ASO

treatment restored the eight affected Nups Nup50, TPR, Nup98, GP210, NDC1, POM121, Nup107, and Nup133 within C9orf72 iPSN nuclei but had no effect on the unaffected Nups Nup153, Nup54, Nup62, Nup93, Nup188, Nup205, and Nup160 (Figures 3A–3T). This finding suggests that observed Nup disruptions are a direct or indirect pathological consequence of the C9orf72 HRE.

To determine whether the ASO-mediated rescue of eight specific Nups within neuronal nuclei could perhaps subsequently impact Ran GTPase localization, we performed immunostaining for endogenous Ran in iPSNs treated with scrambled or sense ASOs for 3 weeks. Similar to our findings with Nups, sense-targeting ASOs restored localization of Ran to the nucleus compared to scrambled controls (Figures 3U and 3V), supporting observations from our previous study that used different iPSC lines and a longer differentiation protocol (Zhang et al., 2015). As a proper Ran GTPase gradient across the nuclear envelope is critical for the maintenance of functional NCT, our data suggest that C9orf72 HRE-targeting ASOs may act to restore the normal Nup levels in nuclei of C9orf72 iPSNs and, in turn, affect NCT. In addition, downstream of the biological effects on Nups and Ran localization, G₄C₂-targeting ASOs mitigated susceptibility to glutamate excitotoxicity in C9orf72 iPSNs (Figure 3W; Figure S13). Collectively, these data suggest that pathologic alterations in the nuclear repertoire of individual NPC components, Ran GTPase localization, and downstream deficits in cellular survival are biological consequences of C9orf72 repeat RNA and/or DPRs.

Overexpression of POM121 Restores the Nuclear Expression of Specific Nups, Localization of Ran GTPase and Fluorescent NCT Reporters, and Protects against Cellular Toxicity

Our data support a model in which only a subset of Nups are reduced from fully assembled NPCs as an underlying pathogenic event in C9orf72-mediated neurodegeneration. To begin to understand the relationship between specific Nups in neurons and in disease, we reintroduced GFP-tagged Nups (Figures S14A and S14B) and used SIM (see STAR Methods for details regarding nuclei selection) to evaluate the localization and levels of individual NPC components. The reintroduction of Nups was conducted at a time point after their initial reduction from the nucleus (30 days; Figure 1). Although overexpression of Nup98 only restored nuclear

Figure 3. Sense-Repeat-RNA-Targeting ASOs Mitigate Alterations in Specific Nups, Restore the Localization of Ran GTPase, and Protect against Cellular Toxicity in C9orf72 iPSNs

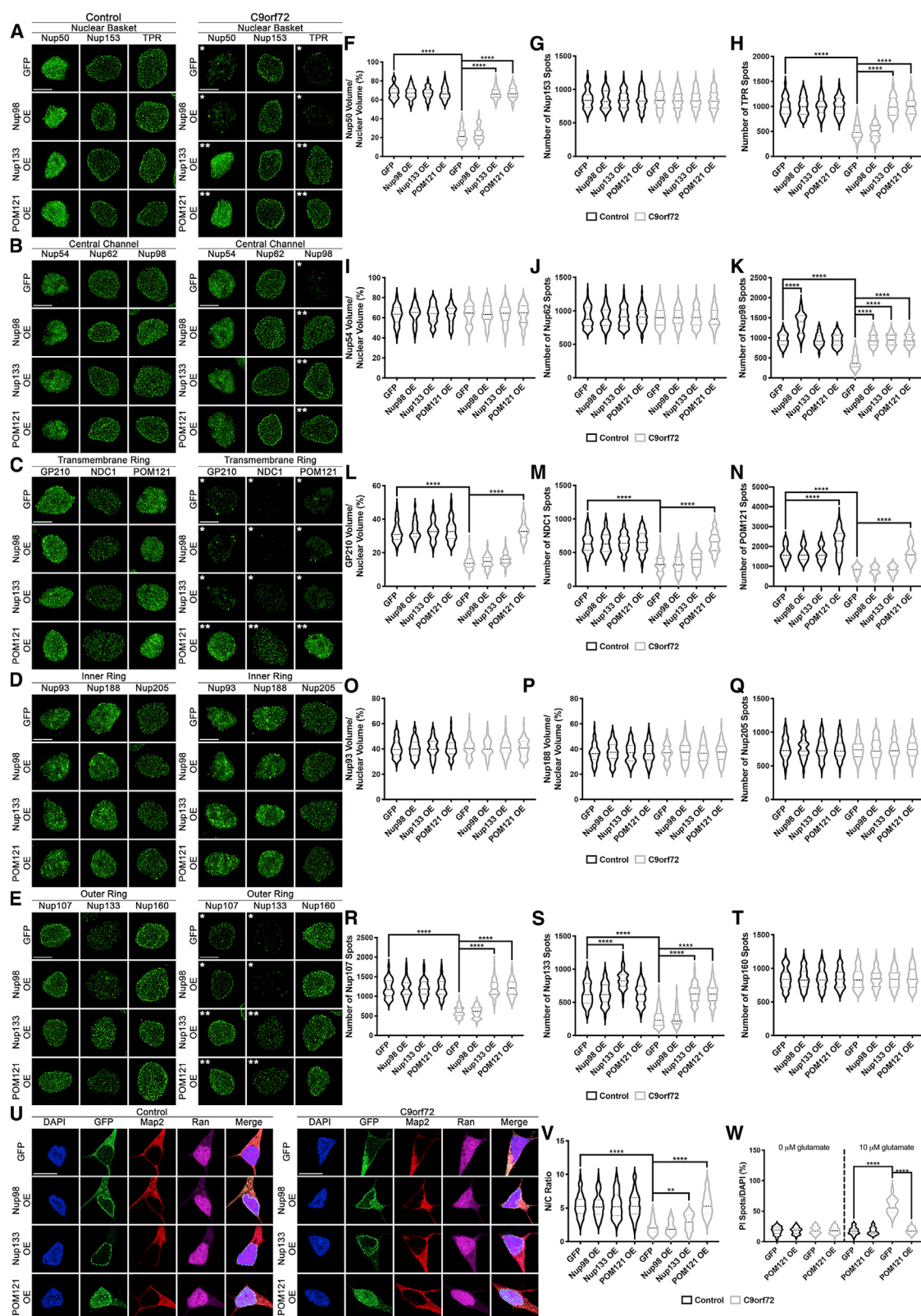
(A–E) Maximum intensity projections from SIM imaging of Nups in nuclei isolated from 5 μM sense-strand-targeting- or scrambled-ASO-treated control and C9orf72 iPSNs. Treatments are indicated on left; genotypes and antibodies are indicated on top.

(F–T) Quantification of Nup spots and volume. n = 5 control and 5 C9orf72 iPSC lines, 50 NeuN+ nuclei per line/treatment. Two-way ANOVA with Tukey multiple comparison test was used to calculate statistical significance. ***p < 0.0001.

(U) Confocal imaging of 5 μM sense-strand targeting- or scrambled-ASO-treated control and C9orf72 iPSNs immunostained for Ran. Treatments are indicated on left; genotypes and antibodies are indicated on top.

(V) Quantification of nuclear-to-cytoplasmic ratio of Ran. n = 3 control and 3 C9orf72 iPSC lines, 30 cells per line. Two-way ANOVA with Tukey multiple comparison test was used to calculate statistical significance. ***p < 0.0001.

(W) Quantification of percent cell death following exposure to glutamate. n = 4 control and 4 C9orf72 iPSC lines, 10 frames per well. Two-way ANOVA with Tukey multiple comparison test was used to calculate statistical significance. ***p < 0.0001. Scale bar, 5 μm (A–E), 10 μm (U). * indicates significantly altered Nups, ** indicates significantly restored Nups.



(legend on next page)

levels of Nup98 (Figures 4A–4T), overexpression of Nup133 restored nuclear levels of Nup50, TPR, Nup98, Nup107, and Nup133 but not GP210, NDC1, and POM121 in C9orf72 iPSNs (Figures 4A–4T). In contrast, overexpression of POM121 variably mitigated all alterations in affected Nups in C9orf72 iPSNs within about 2 weeks (Figures 4A–4T). Interestingly, Nup133 and POM121 overexpression did not alter the total number or distribution of FG-repeat-containing Nups (Figures S14C and S14D).

In contrast to POM121 overexpression, neither a soluble variant of POM121 (sPOM121), which lacks the transmembrane domain and does not localize to the NPC (Franks et al., 2016), nor overexpression of GP210 or NDC1 were able to restore nuclear expression of candidate Nups (Figures S15 and S16). Interestingly, GP210, NDC1, and sPOM121 overexpression all partially restored the nuclear expression of Nup98 (Figures S15A, S15C, S16A, and S16D) suggesting that Nup98 is highly sensitive to a variety of Nup manipulations. Together, these data suggest that NPC-associated POM121 is necessary for the reestablishment of proper nuclear and NPC expression of specific Nups in C9orf72 iPSNs.

In addition to the rescue of nuclear levels of Nups, POM121 overexpression resulted in the relocalization of Ran from the cytoplasm to the nucleus in C9orf72 iPSNs (Figures 4U and 4V). To evaluate whether POM121 overexpression could additionally mitigate defects in the localization of a fluorescent NCT reporter construct, we used the previously characterized lentiviral NLS-tdTomato-NES (S-tdTomato) reporter (Zhang et al., 2015). In this paradigm (Figure S17A), although S-tdTomato is typically predominately nuclear given the strong NLS signal, by 3 days posttransduction, its localization shifts to the cytoplasm in C9orf72 iPSNs (Figures S17B–S17D), indicative of potential disruptions in NCT. However, by 10 days posttransduction, overexpression of POM121 restores the nuclear localization of the S-tdTomato reporter (Figures S17B–S17E) in C9orf72 iPSNs. Moreover, using glutamate-induced cell death assays, we found that POM121 overexpression was sufficient to suppress glutamate-induced excitotoxicity and promoted cellular survival in C9orf72 iPSNs (Figure 4W; Figure S18). Collectively, these data suggest that POM121 overexpression can mitigate alterations in the nuclear expression of specific Nups, the combination of which positively affects nuclear Ran GTPase and S-tdTomato reporter localization and ultimately mitigates downstream cellular toxicity.

Figure 4. POM121 Overexpression Restores the Nuclear Expression of Specific Nups, Localization of Ran GTPase, and Mitigates Cellular Toxicity

(A–E) Maximum intensity projections from SIM imaging of Nups in nuclei isolated from control and C9orf72 iPSNs overexpressing GFP tagged Nup98, Nup133, or POM121. Overexpression is indicated on left; genotypes and antibodies are indicated on top.

(F–T) Quantification of Nup spots and volume. n = 4 control and 4 C9orf72 iPSC lines, 50 GFP+ nuclei per line/overexpression. Two-way ANOVA with Tukey multiple comparison test was used to calculate statistical significance. ***p < 0.0001.

(U) Confocal imaging of control and C9orf72 iPSNs overexpressing GFP-tagged Nup98, Nup133, or POM121 immunostained for Ran. Overexpression is indicated on left; genotypes and antibodies are indicated on top.

(V) Quantification of nuclear-to-cytoplasmic ratio of Ran. n = 4 control and 4 C9orf72 iPSC lines, at least 50 cells per line/overexpression. Two-way ANOVA with Tukey multiple comparison test was used to calculate statistical significance. **p < 0.01, ***p < 0.0001.

(W) Quantification of percent cell death following exposure to glutamate. n = 4 control and 4 C9orf72 iPSC lines, 10 frames per well. Two-way ANOVA with Tukey multiple comparison test was used to calculate statistical significance. ***p < 0.0001. Scale bar, 5 μm (A–E) and 10 μm (U). * indicates significantly altered Nups, ** indicates significantly restored Nups.

Knockdown of POM121 Alone in Wild-type Neurons Recapitulates Disease Phenotypes

Given the variable yet robust phenotypic rescue provided by POM121 overexpression, we hypothesized that a reduction in nuclear POM121 may be an initiating event in C9orf72-mediated disease. Due to the long half-life of many scaffold Nups in neurons (Savas et al., 2012; Toyama et al., 2013), we used the Trim Away method (Clift et al., 2017) to rapidly degrade endogenous Nup133, POM121, NDC1, or GAPDH protein in control iPSNs (Figure S19). Although knockdown of Nup133 resulted in subsequent nuclear reduction of Nup50, TPR, Nup107, and Nup133 (Figures 5A–5P), knockdown of POM121 recapitulated the nuclear decrease in Nup50, TPR, GP210, NDC1, POM121, Nup107, and Nup133 (Figures 5A–5P) observed in C9orf72 iPSNs (Figure 1), human motor cortex (Figure 2), and thoracic spinal cord (Figure S10) within 48 h. Notably, this effect on the levels of Nups in iPSN nuclei was specific to the transmembrane Nup POM121, as Trim21-mediated reduction of the transmembrane Nup NDC1 had no effect on Nups other than itself (Figures 5A–5P). Interestingly, neither Nup133, NDC1, nor POM121 knockdown resulted in disruptions in nuclear-associated Nup98 (Figures 5A–5P). In combination with our overexpression data, these data suggest that Nup98 reduction may be the result of an independent mechanism. Importantly, knockdown of GAPDH, a non-NPC-associated control protein, had no effect on the nuclear expression of any of the 15 Nups analyzed (Figures 5A–5P).

In addition to the nuclear reduction of specific NPC components, knockdown of POM121, but not Nup133 or GAPDH, resulted in Ran GTPase mislocalization from the nucleus to the cytoplasm (Figures 5Q and 5R). Furthermore, Trim21-mediated knockdown of POM121 increased the susceptibility of wild-type neurons to glutamate-induced excitotoxicity (Figures 5S and 5T). Together, these data suggest that nuclear decrease in POM121 can initiate a pathological cascade reminiscent of C9orf72-mediated disease alterations, including disruption of NPC components and downstream effects on Ran GTPase localization and cellular sensitivity to stressors.

Loss of C9ORF72 and DPRs Do Not Contribute to Alterations in the POM121

It has been proposed that the C9orf72 HRE exerts toxicity through the combination of three pathological phenomena including haploinsufficiency of C9ORF72 protein, accumulation of G₄C₂ and G₂C₄ repeat RNA, and production of toxic DPRs

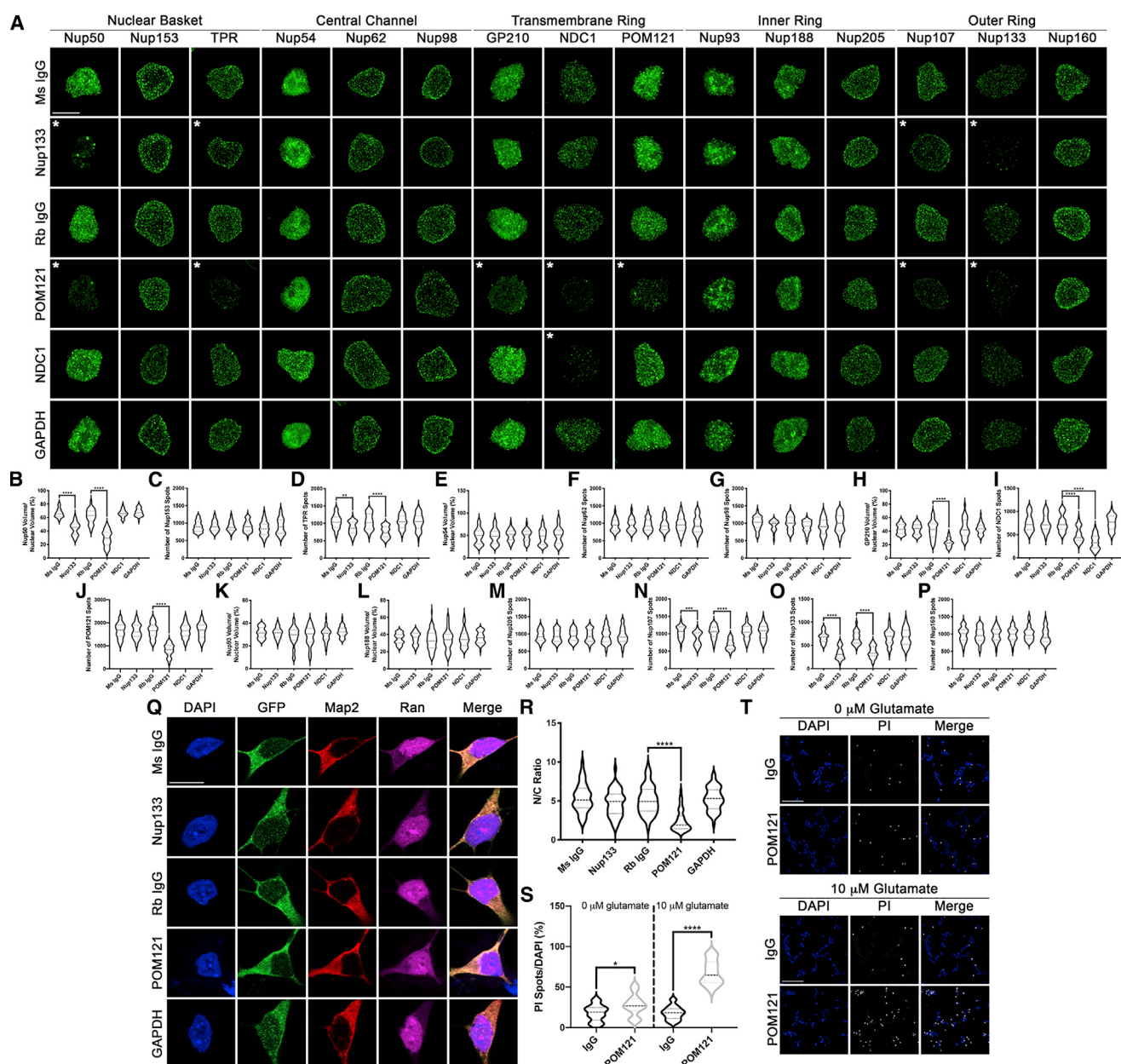


Figure 5. Reduction in POM121 in Wild-type iPSNs Recapitulates C9orf72-Mediated Alterations in Specific Nups and Ran GTPase and Increases Susceptibility to Glutamate-Induced Excitotoxicity

(A–P) Maximum intensity projections from SIM imaging (A) and quantification (B–P) of Nup spots and volume in nuclei isolated from wild-type iPSCs following knockdown of Nup133, POM121, NDC1, or GAPDH. Antibody used for Trim21 GFP-mediated knockdown is indicated on left; antibodies are indicated on top. n = 3 wild-type iPSC lines, 50 GFP+ nuclei per line/knockdown. One-way ANOVA with Tukey multiple comparison test was used to calculate statistical significance. **p < 0.01, ***p < 0.001, ****p < 0.0001.

(Q) Confocal imaging of control iPSCs following Trim21 GFP knockdown of Nup133, POM121, or GAPDH immunostained for Ran. Antibody used for Trim21 knockdown is indicated on left; antibodies are indicated on top.

(R) Quantification of nuclear-to-cytoplasmic ratio of Ran. n = 3 wild-type iPSC lines, at least 50 cells per line/knockdown. One-way ANOVA with Tukey multiple comparison test was used to calculate statistical significance. ****p < 0.0001.

(S) Quantification of percent cell death following exposure to glutamate. n = 3 control iPSC lines, 10 frames per well. Two-way ANOVA with Tukey multiple comparison test was used to calculate statistical significance. ****p < 0.0001.

(T) Confocal imaging of cell death in control and C9orf72 iPSCs as measured by propidium iodide (PI) incorporation. Antibody used for Trim21 is indicated on left; glutamate concentration and stain are indicated on top. Scale bar, 5 μm (A), 10 μm (Q), and 100 μm (T). * indicates significantly altered Nups.

(Balendra and Isaacs, 2018; Cook and Petrucelli, 2019; Gitler and Tsuji, 2016). Although we do not observe a reduction in the C9ORF72 protein in our iPSN model (Figures S1F and S1G), we first used a *C9orf72* knockout (*C9orf72*^{-/-}) iPSC line to investigate whether the complete loss of the C9ORF72 protein affected the nuclear expression of individual Nups. Using SIM, we found that none of the 22 Nups assessed were altered in nuclei isolated from *C9orf72*^{-/-} iPSNs compared to controls (Figures 6A and 6B), suggesting that the loss of the C9ORF72 protein does not play a role in Nup alterations in *C9orf72* ALS.

Multiple studies have reported that artificial overexpression of DPRs produced by the *C9orf72* HRE can result in disruptions in NCT, potentially by cytoplasmic mislocalization and aggregation of a subset of NPC-associated proteins and Nups (Chew et al., 2019; Shi et al., 2017; Zhang et al., 2016, 2018, 2019b). Although we did not observe this pathology in iPSNs (Figure S5C) or post-mortem human tissue (Figure S11), we nonetheless used SIM to evaluate whether overexpression of individual DPRs in wild-type iPSNs affected nuclear expression of POM121. Both Poly(GR) and Poly(PR) strongly accumulates in and/or around the nucleus, whereas nuclear localization of Poly(GA) was rarely observed (Figure 6C). However, neither Poly(GA), Poly(GR), nor Poly(PR) affected the expression or distribution of POM121 within nuclei after 48 h (Figures 6C and 6D) or 1 week (Figures 6C and 6E) of overexpression. These data indicate that like the loss of the C9ORF72 protein, DPRs are not responsible for the initiation of POM121 reduction from human neuronal nuclei during *C9orf72* disease pathogenesis.

Expression of G₄C₂ Repeat RNA Results in Reduced POM121 within Nuclei in iPSNs

To test whether pathological G₄C₂ repeat RNA was responsible for the decreased POM121, we first treated control and *C9orf72* iPSNs with G₄C₂-targeting ASOs for only 5 days beginning at day 30 of differentiation. After 5 day treatment with ASO, we observed a large reduction in G₄C₂ repeat RNA (Figure 7A) but not the Poly(GP) DPR (Figure 7B) indicating that this short ASO treatment paradigm can selectively reduce pathologic repeat RNA but not DPRs, consistent with our previous reports that it takes about 3 weeks to reduce Poly(GP) levels in iPSNs (Gendron et al., 2017). Interestingly, using SIM, we found that this 5-day ASO treatment mitigated the reduced nuclear expression of POM121 in *C9orf72* iPSN nuclei compared to untreated and scrambled ASO controls (Figures 7C and 7D).

As an additional assessment to confirm the effects of G₄C₂ repeat RNA on nuclear expression of POM121, we transfected wild-type iPSNs with stop-codon-optimized constructs that produce G₄C₂ repeat RNA and generate pathologic RNA foci, but not DPRs, in immortalized cell lines (Mizielinska et al., 2014) and iPSNs (Figure S20). Notably, RNA foci were only produced in ~15% of iPSNs (Figures S20A and S20B). This finding is consistent with prior iPSN studies (Donnelly et al., 2013) and human pathology (DeJesus-Hernandez et al., 2017), for which only a subset of neurons contain foci despite the notion that every patient neuron expresses the *C9orf72* HRE. Using SIM, we found that overexpression of 106 or 288, but not 36, G₄C₂ RNA repeats in wild-type iPSNs resulted in a variable reduction in the nuclear expression of POM121 after 2 and 7 days of G₄C₂

repeat RNA expression (Figures 7E–7I). Importantly, overexpression of CGG and CTG repeat RNAs (which cause Fragile X and DM1 muscular dystrophy, respectively) for 7 days in iPSNs did not induce a decrease in POM121 within the nucleus (Figure S21). Together, these data suggest that the reduced nuclear expression of POM121 in spinal neurons is a specific effect of pathological G₄C₂ repeat RNA.

To assess the contribution of G₄C₂ repeat RNA itself to cell death, we performed glutamate toxicity assays. Treatment of *C9orf72* iPSNs with sense-targeting ASOs for 5 days mitigated susceptibility to glutamate-induced excitotoxicity (Figure 7J; Figure S22A), whereas overexpression of 106 or 288 RNA repeats in wild-type iPSNs variably but significantly increased susceptibility to glutamate-induced excitotoxicity (Figure 7K; Figure S22B), mirroring the effects on POM121. Collectively, these data suggest that by direct or indirect mechanisms, G₄C₂ repeat RNA, but not DPRs or a loss of the C9ORF72 protein, initiates a pathological cascade affecting nuclear expression of POM121 and subsequent cellular toxicity in human neurons.

DISCUSSION

Multiple studies have identified nuclear or cytoplasmic mislocalization and accumulation of some NPC-associated proteins in various model systems (Chew et al., 2019; Eftekhari-Zadeh et al., 2018; Hutten and Dommann, 2019; Zhang et al., 2015; 2016, 2018, 2019b). However, many of these reports simply provide an overview of Nup pathology and have focused on a handful of individual Nups or NCT-associated proteins. To date, few studies have linked cytoplasmic Nup accumulations to alterations within the nucleus, nuclear envelope, and NPC itself. Thus, a comprehensive evaluation of the expression and localization of individual Nups within the nucleus and NPCs is lacking. Moreover, the mechanisms by which Nup alterations arise in human CNS cell types remain elusive.

Nucleoporin Alterations in *C9orf72* ALS/FTD

To evaluate the nuclear distribution and expression of most individual human Nups, we harnessed the power and resolution of SIM. Here, we studied >1,000,000 nuclei and comprehensively assessed the actual nuclear repertoire of NPC components in nuclei from iPSNs as well as in postmortem human nervous system tissue from patients harboring the *C9orf72* HRE. We found that 8 of the 23 Nups analyzed are reliably and reproducibly, albeit variably, reduced within human neuronal nuclei in a large number of different *C9orf72* patient iPSN lines (Figure 1) and postmortem human motor cortex (Figure 2) and spinal cord (Figure S10) without corresponding cytoplasmic mislocalization (Figures S5 and S11).

Notably, the stable NPC structure is formed early in cellular development and some of its individual Nup components are extremely long lived, having half-lives measured in years (Savas et al., 2012; Toyama et al., 2013). The evaluation of Nups at multiple time points in the lifespan of our iPSNs reveals that initial nuclear expression of individual Nups is not disrupted by the *C9orf72* HRE, but there is an age-related decrease in specific Nups from the nucleus (Figure 1). Although expression profiles

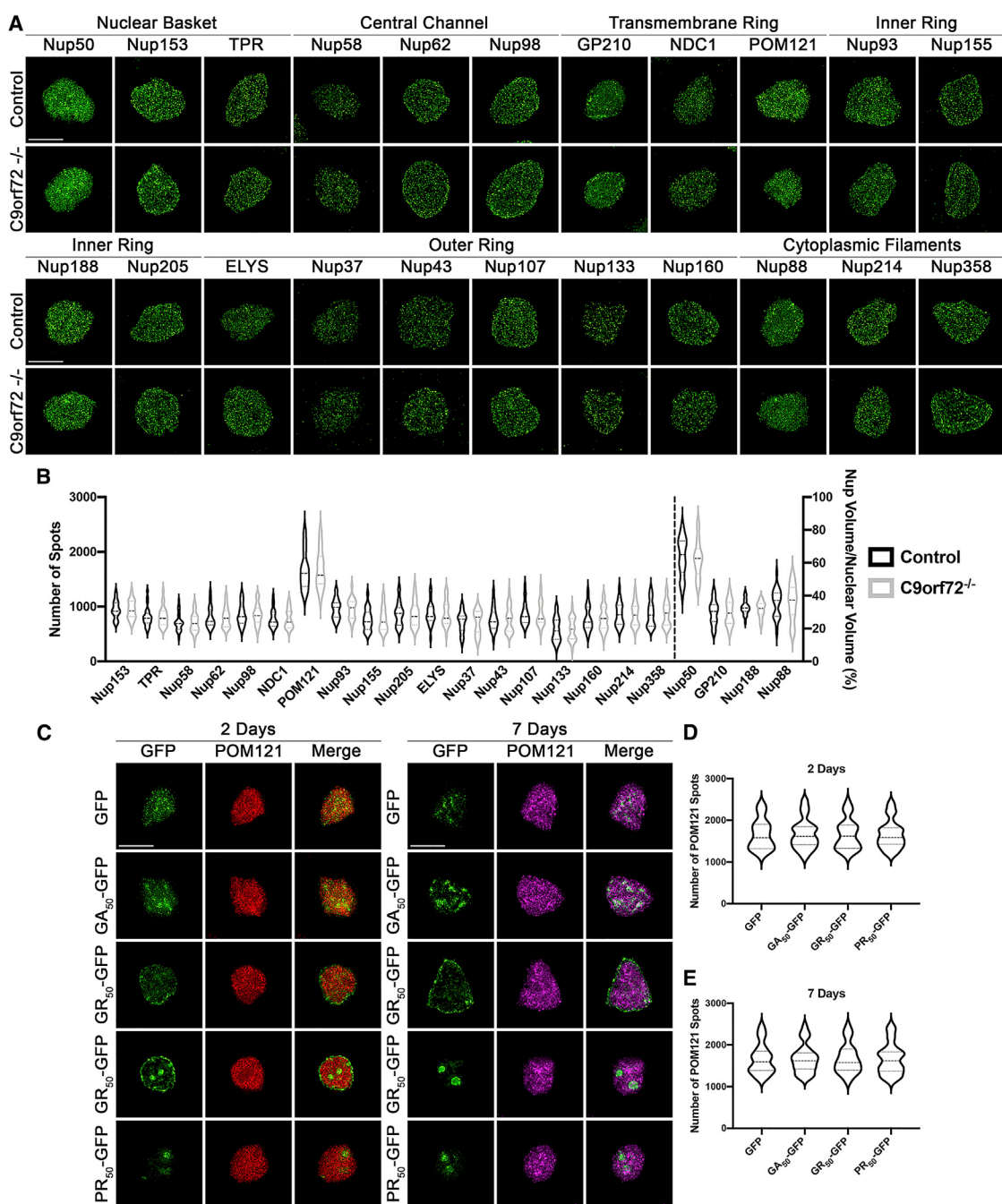


Figure 6. Loss of C9ORF72 Protein or Overexpression of DPRs Does Not Alter the Nuclear Expression of POM121

(A) Maximum intensity projections from SIM imaging of Nups in nuclei isolated from control and C9orf72^{-/-} iPSCs. Genotypes are indicated on left; antibodies are indicated on top.

(B) Quantification of Nup spots and volume. n = 1 control and 1 C9orf72 null line, differentiations conducted in triplicate, 50 NeuN+ nuclei per line/differentiation. Two-way ANOVA with Tukey multiple comparison test was used to calculate statistical significance.

(C) SIM imaging of POM121 in nuclei isolated from wild-type iPSCs overexpressing GFP-tagged Poly(GA), Poly(GR), and Poly(PR) DPRs. Overexpression is indicated on left; antibodies and time points are indicated on top.

(D and E) Quantification of POM121 spots 2 days (D) and 7 days (E) after overexpression of DPRs. n = 3 wild-type iPSC lines, 50 GFP+ nuclei per line/over-expression. One-way ANOVA with Tukey multiple comparison test was used to calculate statistical significance. Scale bar, 5 μm.

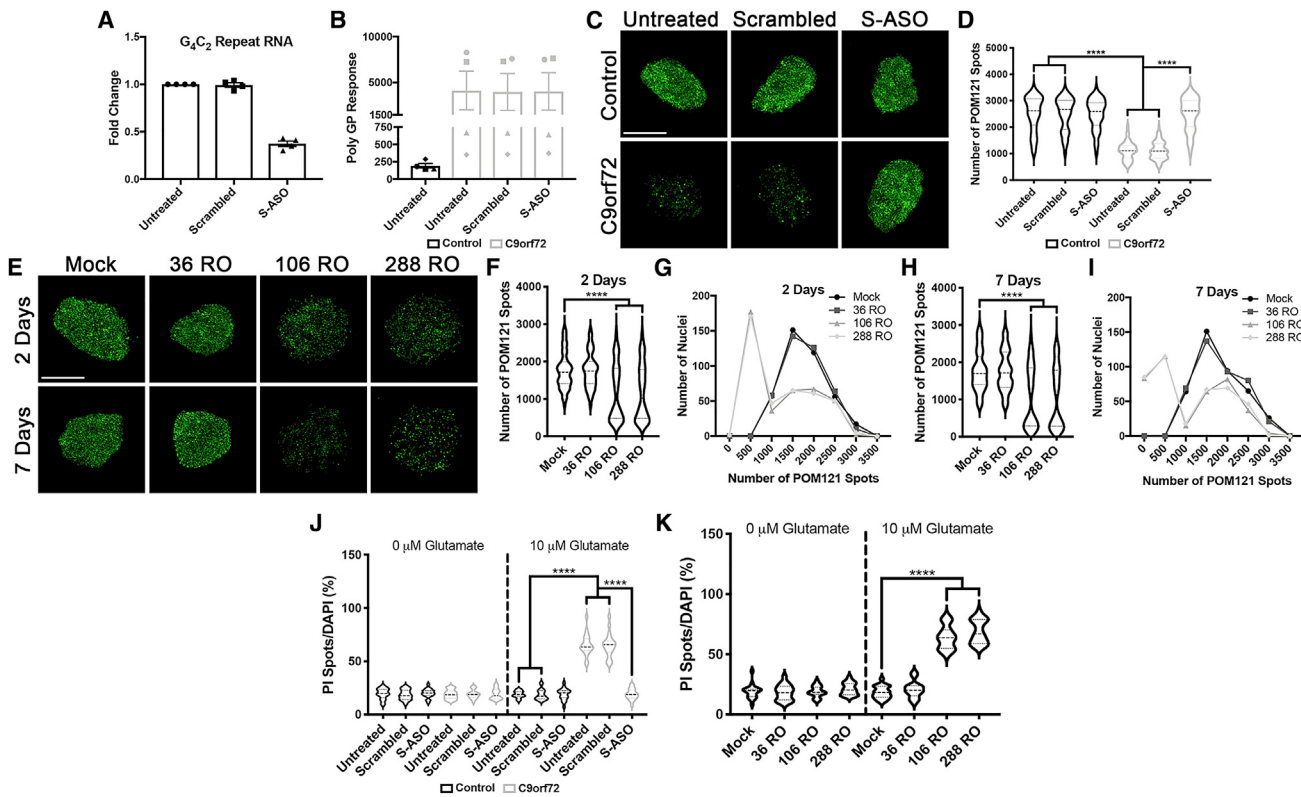


Figure 7. Expression of Pathologic G₄C₂ Repeat RNA Initiates the Nuclear Reduction in POM121

(A and B) qRT-PCR for G₄C₂ repeat RNA (A) and meso scale discovery (MSD) ELISA for Poly(GP) DPR levels (B) in C9orf72 iPSNs following 5 days of treatment with G₄C₂ targeting ASO.

(C) Maximum intensity projections from SIM imaging for POM121 in nuclei isolated from control and C9orf72 iPSNs. Genotypes are indicated on left; treatments are indicated on top.

(D) Quantification of POM121 spots following 5 days of treatment with G₄C₂ targeting ASO. n = 4 control and 4 C9orf72 iPSC lines, 50 NeuN+ nuclei per line/treatment. Two-way ANOVA with Tukey multiple comparison test was used to calculate statistical significance. ***p < 0.0001.

(E) Maximum intensity projections from SIM imaging of POM121 in nuclei isolated from wild-type iPSNs overexpressing 36, 106, or 288 G₄C₂ RNA repeats. Time points are indicated on left; overexpression is indicated on top.

(F–I) Quantification and histogram distributions of POM121 spots 2 days (F and G) and 7 days (H and I) after overexpression of G₄C₂ repeat RNA. n = 4 wild-type iPSC lines, 100 NeuN+ nuclei per line/overexpression. One-way ANOVA with Tukey multiple comparison test was used to calculate statistical significance. ***p < 0.0001.

(J) Quantification of percent cell death following exposure to glutamate in iPSNs treated with ASOs for 5 days. n = 4 control and 4 C9orf72 iPSC lines, 10 frames per well. Two-way ANOVA with Tukey multiple comparison test was used to calculate statistical significance. ***p < 0.0001.

(K) Quantification of percent cell death following exposure to glutamate in wild-type iPSNs overexpressing G₄C₂ repeat RNA. n = 4 control iPSC lines, 10 frames per well. Two-way ANOVA with Tukey multiple comparison test was used to calculate statistical significance. ***p < 0.0001. Scale bar, 5 μm.

and synaptic physiology of iPSNs more closely resemble those of young and immature fetal neurons (Ho et al., 2016), the age dependence (day 18 to day 32) of our observed alterations in specific Nups highlights the ability of our iPSN system to capture the maturation of early pathogenic cascades in C9orf72-mediated neurodegeneration. Importantly, our iPSNs are not dying in culture without the addition of exogenous stressors, and therefore, the alterations in NPC components are not merely reflective of cell death cascades.

Although all three Nups of the transmembrane ring (GP210, NDC1, and POM121) show decreased nuclear expression, the remainder of the disrupted Nups span across multiple domains of the NPC, including the nuclear basket (Nup50 and TPR), central channel (Nup98), and outer ring (Nup107 and Nup133). Collectively, these Nups are involved in both maintaining the

structural integrity and the function of the NPC, as well as NPC-independent nuclear functions (Lin and Hoelz, 2019; Raires and D'Angelo, 2012). As a result, this suggests that the combined C9orf72-mediated alterations in individual NPC components themselves are likely to affect multiple cellular processes, likely including both NCT and gene expression.

Interestingly, the composition of NPCs reportedly vary among cell types and each NPC within a single nucleus in a given cell can vary as individual Nups are replaced (Kinoshita et al., 2012; Rajoo et al., 2018; Toyama et al., 2018). This phenomenon of NPC heterogeneity within individual nuclei may explain differences in Nup staining patterns. Indeed, in accordance with this hypothesis, using SIM, we observe heterogeneity of Nup immunostaining within human iPSN nuclei (Figure S2). Importantly, primary antibodies for this study were selected on the basis of use

in prior publications and/or knockdown validation, as indicated on the manufacturer website (see **Tables S5** and **S6** for additional information). However, the possibility remains that some Nup signals are moderately non-specific or are the result of partial cross reactivity with other nuclear proteins. Nevertheless, these caveats do not undermine the consistent, although variable, observation that a subset of Nups are reproducibly reduced within human C9orf72 neuronal nuclei *in vitro* and *in vivo*, as evaluated by multiple experimental methods and antibodies across multiple patient tissue samples and iPSC lines (see **Tables S1**, **S2**, and **S6**).

Recently, it has been shown that the stoichiometry of Nups within NPCs vary across cell types (Ori et al., 2013; Rajoo et al., 2018). Due to the limitations of SIM, future experiments will be needed to determine the exact stoichiometry of individual Nups within human neurons and NPCs. However, using SEM, we show that the overall distribution and architecture of NPCs in the nuclear envelope of C9orf72 iPSCs remains intact (**Figure S8D**) despite an average reduction of 50% for eight individual Nups (**Figure 1E**). Although arranged into a highly organized octet structure, the NPC itself can be comprised of multiple copies (e.g., 8, 16, and 32) of each individual Nup (Hampoelz et al., 2019; Kim et al., 2018; Lin and Hoelz, 2019). Although SIM provides for increased resolution in detecting individual spots within isolated nuclei, it remains an open question as to whether these spots represent single or multiple Nup molecules within an NPC. As a result, we propose a scenario whereby a variable number of individual Nup molecules may be missing in each NPC without causing the collapse of the whole structure (see **Figure S7B**). Additionally, we cannot rule out the possibility that some Nup spots detected by SIM are not associated with the NPC. Specific Nups have been shown to localize within the nucleus for NPC-independent functions in gene expression and cell division (Raices and D'Angelo, 2012). Although human neurons are no longer dividing, it is possible that a subset of Nup spots detected by SIM are not associated with the NPC itself. The methods to reliably detect reduction of a selected Nup from an individual NPC in human iPSCs remain unclear at this time.

Nuclear Reduction of POM121 as an Initiating Pathological Event in C9orf72 ALS/FTD

As opposed to maintenance pathways, the coordinated assembly of the NPC during mitosis and interphase in dividing cells and yeast is more frequently studied (Lin and Hoelz, 2019; Otsuka and Ellenberg, 2018). To begin to investigate Nup relationships and NPC maintenance in human neurons, we overexpressed candidate Nups from multiple domains of the NPC. Using two independent GFP-tagged POM121 overexpression plasmids, we show that reintroduction of this transmembrane Nup variably re-established the nuclear levels of individual Nups (**Figures 4A–4T**; **Figure S15**; **Table S7**) in C9orf72 iPSCs. Consistent with previous reports indicating that POM121 insertion into the nuclear envelope is a critical initiating event in NPC assembly during interphase (Antonin et al., 2005; Doucet et al., 2010; Funakoshi et al., 2011; Talamas and Hetzer, 2011), our data suggest that in human neurons, POM121 is critical for mediating the nuclear levels of individual Nups.

Together, our overexpression and knockdown experiments suggest that nuclear reduction of the transmembrane Nup POM121 is an initiating event in specific Nup alterations in human C9orf72 neurodegeneration. Reduced POM121 alters the human neuronal nuclear repertoire of Nups, and it is likely the combinatorial effect of these changes affects the subcellular distribution of Ran GTPase. Among other possibilities, disruption of the Ran localization may be the result of alterations to Nups directly involved in NCT and/or a result of potential disruptions in gene transcription that may ultimately impact NCT. Future studies are necessary to define the effect of individual Nup alterations on neuronal gene expression and specific aspects of functional NCT, including those involving NTRs and cargo loading/unloading. Collectively, the combined loss of eight specific Nups and mislocalization of Ran GTPase are likely to affect multiple cellular pathways, the combination of which renders human neurons susceptible to stressor-mediated cell death.

G₄C₂-Repeat-RNA-Mediated Reduction of POM121 and Initiation of NPC Deficits in Human Neurons

It has previously been shown that Nups can modify C9orf72 toxicity in *Drosophila* photoreceptors (Freibaum et al., 2015), and it has been proposed that pathologic DPRs produced by the C9orf72 HRE can interact with Nups to disrupt NCT (Lee et al., 2016; Shi et al., 2017). Although in the current study overexpression of DPRs does not negatively affect POM121, the possibility remains that DPRs may directly affect the localization of other NPC components (e.g., Nup98 and NPC-associated proteins). Furthermore, it is possible that DPRs may directly contribute to Nup-independent alterations in functional NCT, potentially by pathologic associations with NTRs that have previously been identified as strong DPR interactors (Lee et al., 2016). Indeed, recent work from our lab shows that arginine-rich DPRs Poly(GR) and Poly(PR) can directly interfere with importin beta function in non-neuronal systems (Hayes et al., 2020). As a result, DPR-dependent effects on the NCT machinery itself may further compound alterations in NCT that arise as a result of compromised nuclear expression of Nups. This could suggest a two-hit model for disruptions in NCT in C9orf72 ALS/FTD.

We provide multiple lines of evidence suggesting that the expression of G₄C₂ repeat RNA initiates the deficit in nuclear Nup levels (**Figure 7**; **Figure S21**; **Table S9**). Notably, these results differ from previous studies in dividing cells or fly models overexpressing only G₄C₂ repeat RNA where no overt toxicity or degeneration was observed (Mizielinska et al., 2014). In the context of our current study in human spinal neurons, we note that flies do not have a gene encoding a POM121 ortholog and, thus, would not be susceptible to this RNA-mediated pathologic event. Moreover, we have been unable to observe POM121 reduction in BAC C9orf72 and AAV-(G₄C₂)₁₄₉ mouse models (unpublished data). However, we note that human and mouse POM121 only share ~60% protein sequence homology that may not be sufficient for this toxic G₄C₂-repeat-RNA-mediated event to occur. Interestingly, nucleofection of even very low amounts of G₂C₄-repeat-RNA-only plasmid constructs (anti-sense strand; generously provided by A. Isaacs) resulted in complete lethality of iPSCs within 24 h (unpublished data). Future

studies are warranted to explore the mechanisms underlying this robust G₂C₄-repeat-RNA-mediated neuronal toxicity.

Although the reduction in nuclear POM121 levels is specific to the expression of G₄C₂ repeat RNA in spinal neurons (Figure 7; Figure S21; Table S9), it still remains possible that CGG and/or CTG repeat RNAs can elicit similar deficits when expressed in their disease-specific neuronal subtype. In addition, we do not observe a decrease in the nuclear levels of POM121 in human iPSC-derived astrocyte nuclei or oligodendrocyte nuclei from the postmortem motor cortex (Figures S23A–S23D). Moreover, overexpression of G₄C₂ repeat RNA in human astrocytes and HEK293T cells has no effect on the nuclear expression of POM121 (Figures S23E–S23H). Together, these data support a role for the cell-type-specific nature of G₄C₂ repeat RNA in the initiation of pathogenic Nup disruption specifically in disease-relevant human neuronal subtypes. Given that G₄C₂ repeat RNA foci are rarely observed in iPSCs and patient tissue (DeJesus-Hernandez et al., 2017; Donnelly et al., 2013), future experiments are necessary to determine if reduced nuclear POM121 is the result of direct interactions between POM121 and soluble or foci-accumulated G₄C₂ or G₂C₄ RNA. Although we have repeatedly attempted to perform fluorescence *in situ* hybridization (FISH) and immunofluorescence (IF) to address the possibility of an interaction between RNA foci and POM121, these experiments are technically challenging in iPSC systems and were unrevealing. Alternatively, it is equally possible that indirect interactions by intermediate proteins and/or RNAs may contribute to G₄C₂-repeat-RNA-mediated POM121 reduction. Our previous work did not identify POM121 as a direct interactor of G₄C₂ repeat RNA (Zhang et al., 2015), suggesting that C9orf72 HRE-mediated effects on the nuclear expression of POM121 could be due to indirect interactions between G₄C₂ repeat RNA and POM121 and may involve currently unidentified proteins and/or RNAs.

Collectively, our data support a role for G₄C₂ repeat RNA in early pathogenic disruptions in ALS. Furthermore, our data highlight the importance of POM121 in the initiating events leading to overall disruptions in nuclear Nup levels, Ran GTPase localization, and downstream impaired cellular survival in the pathogenesis of C9orf72 ALS/FTD within human neurons.

STAR★METHODS

Detailed methods are provided in the online version of this paper and include the following:

- KEY RESOURCES TABLE
- RESOURCE AVAILABILITY
 - Lead Contact
 - Materials Availability
 - Data and Code Availability
- EXPERIMENTAL MODEL AND SUBJECT DETAILS
 - iPSC Neuron Differentiation
 - Human Tissue Immunofluorescence
- METHOD DETAILS
 - ASO Treatment of iPSC Derived Neurons
 - RT-qPCR
 - Actinomycin D Treatment

- Polyribosome Fractionation
- Meso Scale Discovery (MSD) ELISA
- Western Blots
- Nuclei Isolation and Super Resolution Structured Illumination Microscopy
- Immunofluorescent Staining and Confocal Imaging
- Plasmids and Nucleofection for Nup, G₄C₂ repeat RNA, and DPR Overexpression
- Knockdown of Nups by Trim Away
- NLS-tdTomato-NES (S-tdTomato) Nucleocytoplasmic Transport Assay
- Glutamate Toxicity
- Scanning Electron Microscopy
- Dextran Exclusion
- RNA FISH
- Evaluation of POM121 in Astroglia, Oligodendroglia, and HEK293T Cells

● QUANTIFICATION AND STATISTICAL ANALYSIS

SUPPLEMENTAL INFORMATION

Supplemental Information can be found online at <https://doi.org/10.1016/j.neuron.2020.06.027>.

ACKNOWLEDGMENTS

We thank the ALS patients and their families for essential contributions to this research and the Target ALS Human Postmortem Tissue Core and Jonathan Glass (Emory University; ADRC NIH P50 AG025688-11REV) for providing postmortem human tissue. We also thank Martin Hetzer, Adrian Isaacs, Davide Trotti, and Maurice Swanson for kindly gifting POM121, G₄C₂ RNA Only, DPR, and (CTG)₂₀₂ plasmids, respectively. Expert technical assistance for iPSC maintenance was provided by Xiaopei Tang and Weibo Zhou. We thank Patrick Lusk for helpful comments in the editing of this manuscript. This work was supported by the ALSA Milton Safenowitz Postdoctoral Fellowship (ANC), a research grant from the Israel Science Foundation (958/15) to A.H., and with funding to J.D.R. from NIH-NINDS (RF1AG062171, P01NS099114, and R01NS094239), The Robert Packard Center for ALS Research Answer ALS Program, ALS Finding a Cure, ALS Association, Muscular Dystrophy Association, F Prime, and the Chan Zuckerberg Initiative.

AUTHOR CONTRIBUTIONS

Conceived and designed the experiments: A.N.C. and J.D.R. Performed the experiments: A.N.C., B.L.Z., L.H., B.F., E.-C.L., and H.T. Analyzed the data: A.N.C., Y.S., K.B., H.T., D.S., and J.D.R. Contributed reagents and materials: A.N.C., B.L.Z., L.H., S.A., F.R., D.S., C.N.S., G.W.Y., A.H., and J.D.R. Wrote the manuscript: A.N.C. and J.D.R. with input from co-authors.

DECLARATIONS OF INTERESTS

The authors declare no competing interests.

Received: July 19, 2019

Revised: March 6, 2020

Accepted: June 23, 2020

Published: July 15, 2020

REFERENCES

- Ababneh, N.A., Scaber, J., Flynn, R., Douglas, A., Barbagallo, P., Candalija, A., Turner, M.R., Sims, D., Dafinca, R., Cowley, S.A., and Talbot, K. (2020). Correction of amyotrophic lateral sclerosis related phenotypes in induced pluripotent stem cell-derived motor neurons carrying a hexanucleotide

- expansion mutation in C9orf72 by CRISPR/Cas9 genome editing using homology-directed repair. *Hum. Mol. Genet.* ddaa106.
- Antonin, W., Franz, C., Haselmann, U., Antony, C., and Mattaj, J.W. (2005). The integral membrane nucleoporin pom121 functionally links nuclear pore complex assembly and nuclear envelope formation. *Mol. Cell* 17, 83–92.
- Balendra, R., and Isaacs, A.M. (2018). C9orf72-mediated ALS and FTD: multiple pathways to disease. *Nat. Rev. Neurol.* 14, 544–558.
- Beck, M., and Hurt, E. (2017). The nuclear pore complex: understanding its function through structural insight. *Nat. Rev. Mol. Cell Biol.* 18, 73–89.
- Cheng, W., Wang, S., Zhang, Z., Morgens, D.W., Hayes, L.R., Lee, S., Portz, B., Xie, Y., Nguyen, B.V., Haney, M.S., et al. (2019). CRISPR-Cas9 Screens Identify the RNA Helicase DDX3X as a Repressor of C9ORF72 (GGGGCC) Repeat-Associated Non-AUG Translation. *Neuron* 104, 885–898.e8.
- Chew, J., Cook, C., Gendron, T.F., Jansen-West, K., Del Rosso, G., Daugherty, L.M., Castanedes-Casey, M., Kurti, A., Stankowski, J.N., Disney, M.D., et al. (2019). Aberrant deposition of stress granule-resident proteins linked to C9orf72-associated TDP-43 proteinopathy. *Mol. Neurodegener.* 14, 9.
- Chou, C.C., Zhang, Y., Umoh, M.E., Vaughan, S.W., Lorenzini, I., Liu, F., Sayegh, M., Donlin-Asp, P.G., Chen, Y.H., Duong, D.M., et al. (2018). TDP-43 pathology disrupts nuclear pore complexes and nucleocytoplasmic transport in ALS/FTD. *Nat. Neurosci.* 21, 228–239.
- Clift, D., McEwan, W.A., Labzin, L.I., Konieczny, V., Mogessie, B., James, L.C., and Schuh, M. (2017). A Method for the Acute and Rapid Degradation of Endogenous Proteins. *Cell* 171, 1692–1706.e1618.
- Cook, C., and Petrucelli, L. (2019). Genetic Convergence Brings Clarity to the Enigmatic Red Line in ALS. *Neuron* 101, 1057–1069.
- Dafinca, R., Scaber, J., Ababneh, N., Lalic, T., Weir, G., Christian, H., Vowles, J., Douglas, A.G., Fletcher-Jones, A., Browne, C., et al. (2016). C9orf72 Hexanucleotide Expansions Are Associated with Altered Endoplasmic Reticulum Calcium Homeostasis and Stress Granule Formation in Induced Pluripotent Stem Cell-Derived Neurons from Patients with Amyotrophic Lateral Sclerosis and Frontotemporal Dementia. *Stem Cells* 34, 2063–2078.
- D'Angelo, M.A., Raices, M., Panowski, S.H., and Hetzer, M.W. (2009). Age-dependent deterioration of nuclear pore complexes causes a loss of nuclear integrity in postmitotic cells. *Cell* 136, 284–295.
- DeJesus-Hernandez, M., Mackenzie, I.R., Boeve, B.F., Boxer, A.L., Baker, M., Rutherford, N.J., Nicholson, A.M., Finch, N.A., Flynn, H., Adamson, J., et al. (2011). Expanded GGGGCC hexanucleotide repeat in noncoding region of C9ORF72 causes chromosome 9p-linked FTD and ALS. *Neuron* 72, 245–256.
- DeJesus-Hernandez, M., Finch, N.A., Wang, X., Gendron, T.F., Bieniek, K.F., Heckman, M.G., Vasilevich, A., Murray, M.E., Rousseau, L., Weesner, R., et al. (2017). In-depth clinico-pathological examination of RNA foci in a large cohort of C9ORF72 expansion carriers. *Acta Neuropathol.* 134, 255–269.
- Donnelly, C.J., Zhang, P.W., Pham, J.T., Haeusler, A.R., Mistry, N.A., Vidensky, S., Daley, E.L., Poth, E.M., Hoover, B., Fines, D.M., et al. (2013). RNA toxicity from the ALS/FTD C9ORF72 expansion is mitigated by antisense intervention. *Neuron* 80, 415–428.
- Doucet, C.M., Talamas, J.A., and Hetzer, M.W. (2010). Cell cycle-dependent differences in nuclear pore complex assembly in metazoa. *Cell* 141, 1030–1041.
- Eftekharpazadeh, B., Daigle, J.G., Kapinos, L.E., Coyne, A., Schiantarelli, J., Carlomagno, Y., Cook, C., Miller, S.J., Dujardin, S., Amaral, A.S., et al. (2018). Tau Protein Disrupts Nucleocytoplasmic Transport in Alzheimer's Disease. *Neuron* 99, 925–940.e7.
- Ferrari, R., Kapogiannis, D., Huey, E.D., and Momeni, P. (2011). FTD and ALS: a tale of two diseases. *Curr. Alzheimer Res.* 8, 273–294.
- Fichtman, B., Shaulov, L., and Harel, A. (2014). Imaging metazoan nuclear pore complexes by field emission scanning electron microscopy. *Methods Cell Biol.* 122, 41–58.
- Fichtman, B., Harel, T., Biran, N., Zagairy, F., Applegate, C.D., Salzberg, Y., Gilboa, T., Salah, S., Shaag, A., Simanovsky, N., et al. (2019). Pathogenic Variants in NUP214 Cause "Plugged" Nuclear Pore Channels and Acute Febrile Encephalopathy. *Am. J. Hum. Genet.* 105, 48–64.
- Franks, T.M., Benner, C., Narvaiza, I., Marchetto, M.C., Young, J.M., Malik, H.S., Gage, F.H., and Hetzer, M.W. (2016). Evolution of a transcriptional regulator from a transmembrane nucleoporin. *Genes Dev.* 30, 1155–1171.
- Freibaum, B.D., Lu, Y., Lopez-Gonzalez, R., Kim, N.C., Almeida, S., Lee, K.H., Badders, N., Valentine, M., Miller, B.L., Wong, P.C., et al. (2015). GGGGCC repeat expansion in C9orf72 compromises nucleocytoplasmic transport. *Nature* 525, 129–133.
- Funakoshi, T., Clever, M., Watanabe, A., and Imamoto, N. (2011). Localization of Pom121 to the inner nuclear membrane is required for an early step of interphase nuclear pore complex assembly. *Mol. Biol. Cell* 22, 1058–1069.
- Gasset-Rosa, F., Chillon-Marinas, C., Goginashvili, A., Atwal, R.S., Artates, J.W., Tabet, R., Wheeler, V.C., Bang, A.G., Cleveland, D.W., and Lagier-Tourenne, C. (2017). Polyglutamine-Expanded Huntingtin Exacerbates Age-Related Disruption of Nuclear Integrity and Nucleocytoplasmic Transport. *Neuron* 94, 48–57.e4.
- Gendron, T.F., Chew, J., Stankowski, J.N., Hayes, L.R., Zhang, Y.J., Prudencio, M., Carlomagno, Y., Daugherty, L.M., Jansen-West, K., Perkerson, E.A., et al. (2017). Poly(GP) proteins are a useful pharmacodynamic marker for C9ORF72-associated amyotrophic lateral sclerosis. *Sci. Transl. Med.* 9, eaai7866.
- Gitler, A.D., and Tsujii, H. (2016). There has been an awakening: Emerging mechanisms of C9orf72 mutations in FTD/ALS. *Brain Res.* 1647, 19–29.
- Grima, J.C., Daigle, J.G., Arbez, N., Cunningham, K.C., Zhang, K., Ochaba, J., Geater, C., Morozko, E., Stocksdale, J., Glatzer, J.C., et al. (2017). Mutant Huntingtin Disrupts the Nuclear Pore Complex. *Neuron* 94, 93–107.e6.
- Hampelz, B., Andres-Pons, A., Kastritis, P., and Beck, M. (2019). Structure and Assembly of the Nuclear Pore Complex. *Annu. Rev. Biophys.* 48, 515–536.
- Hayes, L.R., Duan, L., Bowen, K., Kalab, P., and Rothstein, J.D. (2020). C9orf72 arginine-rich dipeptide repeat proteins disrupt karyopherin-mediated nuclear import. *eLife* 9, e51685.
- Hetzer, M.W. (2010). The role of the nuclear pore complex in aging of post-mitotic cells. *Aging (Albany NY)* 2, 74–75.
- Ho, R., Sances, S., Gowing, G., Amoroso, M.W., O'Rourke, J.G., Sahabian, A., Wichterle, H., Baloh, R.H., Sareen, D., and Svendsen, C.N. (2016). ALS disrupts spinal motor neuron maturation and aging pathways within gene co-expression networks. *Nat. Neurosci.* 19, 1256–1267.
- Hutten, S., and Dormann, D. (2019). Nucleocytoplasmic transport defects in neurodegeneration - Cause or consequence? *Semin. Cell Dev. Biol.* 99, 151–162.
- Jovićić, A., Mertens, J., Boeynaems, S., Bogaert, E., Chai, N., Yamada, S.B., Paul, J.W., 3rd, Sun, S., Herdy, J.R., Bieri, G., et al. (2015). Modifiers of C9orf72 dipeptide repeat toxicity connect nucleocytoplasmic transport defects to FTD/ALS. *Nat. Neurosci.* 18, 1226–1229.
- Kim, S.J., Fernandez-Martinez, J., Nudelman, I., Shi, Y., Zhang, W., Raveh, B., Herricks, T., Slaughter, B.D., Hogan, J.A., Upla, P., et al. (2018). Integrative structure and functional anatomy of a nuclear pore complex. *Nature* 555, 475–482.
- Kinoshita, Y., Kalir, T., Dottino, P., and Kohtz, D.S. (2012). Nuclear distributions of NUP62 and NUP214 suggest architectural diversity and spatial patterning among nuclear pore complexes. *PLoS One* 7, e36137.
- Lagier-Tourenne, C., Baughn, M., Rigo, F., Sun, S., Liu, P., Li, H.R., Jiang, J., Watt, A.T., Chun, S., Katz, M., et al. (2013). Targeted degradation of sense and antisense C9orf72 RNA foci as therapy for ALS and frontotemporal degeneration. *Proc. Natl. Acad. Sci. USA* 110, E4530–E4539.
- Lee, K.H., Zhang, P., Kim, H.J., Mitrea, D.M., Sarkar, M., Freibaum, B.D., Cika, J., Coughlin, M., Messing, J., Molleix, A., et al. (2016). C9orf72 Dipeptide Repeats Impair the Assembly, Dynamics, and Function of Membrane-Less Organelles. *Cell* 167, 774–788.e17.
- Li, C., Goryaynov, A., and Yang, W. (2016). The selective permeability barrier in the nuclear pore complex. *Nucleus* 7, 430–446.
- Lin, D.H., and Hoelz, A. (2019). The Structure of the Nuclear Pore Complex (An Update). *Annu. Rev. Biochem.* 88, 725–783.

- Ling, S.C., Polymenidou, M., and Cleveland, D.W. (2013). Converging mechanisms in ALS and FTD: disrupted RNA and protein homeostasis. *Neuron* 79, 416–438.
- Maglione, M., and Sisrist, S.J. (2013). Seeing the forest tree by tree: super-resolution light microscopy meets the neurosciences. *Nat. Neurosci.* 16, 790–797.
- Melchior, F. (2001). Ran GTPase cycle: one mechanism—two functions. *Curr. Biol.* 11, R257–R260.
- Mizielinska, S., Grönke, S., Niccoli, T., Ridler, C.E., Clayton, E.L., Devoy, A., Moens, T., Norona, F.E., Woollacott, I.O.C., Pietrzyk, J., et al. (2014). C9orf72 repeat expansions cause neurodegeneration in Drosophila through arginine-rich proteins. *Science* 345, 1192–1194.
- Nutter, C.A., Bubenik, J.L., Oliveira, R., Ivankovic, F., Szajner, L.J., Kidd, B.M., Pinto, B.S., Otero, B.A., Carter, H.A., Vitriol, E.A., et al. (2019). Cell-type-specific dysregulation of RNA alternative splicing in short tandem repeat mouse knockin models of myotonic dystrophy. *Genes Dev.* 33, 1635–1640.
- Ori, A., Banterle, N., Iskar, M., Andrés-Pons, A., Escher, C., Khanh Bui, H., Sparks, L., Solis-Mezarino, V., Rinner, O., Bork, P., et al. (2013). Cell type-specific nuclear pores: a case in point for context-dependent stoichiometry of molecular machines. *Mol. Syst. Biol.* 9, 648.
- Osborne, R.J., and Thornton, C.A. (2008). Cell-free cloning of highly expanded CTG repeats by amplification of dimerized expanded repeats. *Nucleic Acids Res.* 36, e24.
- Otsuka, S., and Ellenberg, J. (2018). Mechanisms of nuclear pore complex assembly - two different ways of building one molecular machine. *FEBS Lett.* 592, 475–488.
- Pascual-Garcia, P., and Capelson, M. (2019). Nuclear pores in genome architecture and enhancer function. *Curr. Opin. Cell Biol.* 58, 126–133.
- Popken, P., Ghavami, A., Onck, P.R., Poolman, B., and Veenhoff, L.M. (2015). Size-dependent leak of soluble and membrane proteins through the yeast nuclear pore complex. *Mol. Biol. Cell* 26, 1386–1394.
- Raices, M., and D'Angelo, M.A. (2012). Nuclear pore complex composition: a new regulator of tissue-specific and developmental functions. *Nat. Rev. Mol. Cell Biol.* 13, 687–699.
- Rajoo, S., Vallotton, P., Onischenko, E., and Weis, K. (2018). Stoichiometry and compositional plasticity of the yeast nuclear pore complex revealed by quantitative fluorescence microscopy. *Proc. Natl. Acad. Sci. USA* 115, E3969–E3977.
- Renton, A.E., Majounie, E., Waite, A., Simón-Sánchez, J., Rollinson, S., Gibbs, J.R., Schymick, J.C., Laaksovirta, H., van Swieten, J.C., Myllykangas, L., et al. (2011). A hexanucleotide repeat expansion in C9ORF72 is the cause of chromosome 9p21-linked ALS-FTD. *Neuron* 72, 257–268.
- Sances, S., Bruijn, L.I., Chandran, S., Eggan, K., Ho, R., Klim, J.R., Livesey, M.R., Lowry, E., Macklis, J.D., Rushton, D., et al. (2016). Modeling ALS with motor neurons derived from human induced pluripotent stem cells. *Nat. Neurosci.* 19, 542–553.
- Sareen, D., O'Rourke, J.G., Meera, P., Muhammad, A.K., Grant, S., Simpkinson, M., Bell, S., Carmona, S., Ornelas, L., Sahabian, A., et al. (2013). Targeting RNA foci in iPSC-derived motor neurons from ALS patients with a C9ORF72 repeat expansion. *Sci. Transl. Med.* 5, 208ra149.
- Savas, J.N., Toyama, B.H., Xu, T., Yates, J.R., 3rd, and Hetzer, M.W. (2012). Extremely long-lived nuclear pore proteins in the rat brain. *Science* 335, 942.
- Schermelleh, L., Carlton, P.M., Haase, S., Shao, L., Winoto, L., Kner, P., Burke, B., Cardoso, M.C., Agard, D.A., Gustafsson, M.G., et al. (2008). Subdiffraction multicolor imaging of the nuclear periphery with 3D structured illumination microscopy. *Science* 320, 1332–1336.
- Shi, K.Y., Mori, E., Nizami, Z.F., Lin, Y., Kato, M., Xiang, S., Wu, L.C., Ding, M., Yu, Y., Gall, J.G., and McKnight, S.L. (2017). Toxic PR_n poly-dipeptides encoded by the C9orf72 repeat expansion block nuclear import and export. *Proc. Natl. Acad. Sci. USA* 114, E1111–E1117.
- Talamas, J.A., and Hetzer, M.W. (2011). POM121 and Sun1 play a role in early steps of interphase NPC assembly. *J. Cell Biol.* 194, 27–37.
- Taylor, J.P., Brown, R.H., Jr., and Cleveland, D.W. (2016). Decoding ALS: from genes to mechanism. *Nature* 539, 197–206.
- Thevathasan, J.V., Kahnwald, M., Ciesielski, K., Hoess, P., Peneti, S.K., Reitberger, M., Heid, D., Kasuba, K.C., Hoerner, S.J., Li, Y., et al. (2019). Nuclear pores as versatile reference standards for quantitative superresolution microscopy. *Nat. Methods* 16, 1045–1053.
- Timney, B.L., Raveh, B., Mironsko, R., Trivedi, J.M., Kim, S.J., Russel, D., Wente, S.R., Sali, A., and Rout, M.P. (2016). Simple rules for passive diffusion through the nuclear pore complex. *J. Cell Biol.* 215, 57–76.
- Toyama, B.H., Savas, J.N., Park, S.K., Harris, M.S., Ingolia, N.T., Yates, J.R., 3rd, and Hetzer, M.W. (2013). Identification of long-lived proteins reveals exceptional stability of essential cellular structures. *Cell* 154, 971–982.
- Toyama, B.H., Arrojo, E.D.R., Lev-Ram, V., Ramachandra, R., Deerinck, T.J., Lechene, C., Ellisman, M.H., and Hetzer, M.W. (2018). Visualization of long-lived proteins reveals age mosaicism within nuclei of postmitotic cells. *J. Cell Biol.* 218, 433–444.
- Vatsavayai, S.C., Yoon, S.J., Gardner, R.C., Gendron, T.F., Vargas, J.N., Trujillo, A., Pribadi, M., Phillips, J.J., Gaus, S.E., Hixson, J.D., et al. (2016). Timing and significance of pathological features in C9orf72 expansion-associated frontotemporal dementia. *Brain* 139, 3202–3216.
- Waite, A.J., Baumer, D., East, S., Neal, J., Morris, H.R., Ansorge, O., and Blake, D.J. (2014). Reduced C9orf72 protein levels in frontal cortex of amyotrophic lateral sclerosis and frontotemporal degeneration brain with the C9ORF72 hexanucleotide repeat expansion. *Neurobiol. Aging* 35, 1779.e1–1779.e13.
- Wen, X., Tan, W., Westergard, T., Krishnamurthy, K., Markandaiah, S.S., Shi, Y., Lin, S., Shneider, N.A., Monaghan, J., Pandey, U.B., et al. (2014). Antisense proline-arginine RAN dipeptides linked to C9ORF72-ALS/FTD form toxic nuclear aggregates that initiate in vitro and in vivo neuronal death. *Neuron* 84, 1213–1225.
- Zhang, K., Donnelly, C.J., Haeusler, A.R., Grima, J.C., Machamer, J.B., Steinwald, P., Daley, E.L., Miller, S.J., Cunningham, K.M., Vidensky, S., et al. (2015). The C9orf72 repeat expansion disrupts nucleocytoplasmic transport. *Nature* 525, 56–61.
- Zhang, Y.J., Gendron, T.F., Grima, J.C., Sasaguri, H., Jansen-West, K., Xu, Y.F., Katzman, R.B., Gass, J., Murray, M.E., Shinohara, M., et al. (2016). C9ORF72 poly(GA) aggregates sequester and impair HR23 and nucleocytoplasmic transport proteins. *Nat. Neurosci.* 19, 668–677.
- Zhang, Y.J., Gendron, T.F., Ebbert, M.T.W., O'Raw, A.D., Yue, M., Jansen-West, K., Zhang, X., Prudencio, M., Chew, J., Cook, C.N., et al. (2018). Poly(GR) impairs protein translation and stress granule dynamics in C9orf72-associated frontotemporal dementia and amyotrophic lateral sclerosis. *Nat. Med.* 24, 1136–1142.
- Zhang, X., Hu, D., Shang, Y., and Qi, X. (2019a). Using induced pluripotent stem cell neuronal models to study neurodegenerative diseases. *Biochim. Biophys. Acta Mol. Basis Dis.* 1866, 165431.
- Zhang, Y.J., Guo, L., Gonzales, P.K., Gendron, T.F., Wu, Y., Jansen-West, K., O'Raw, A.D., Pickles, S.R., Prudencio, M., Carlonago, Y., et al. (2019b). Heterochromatin anomalies and double-stranded RNA accumulation underlie C9orf72 poly(PR) toxicity. *Science* 363, eaav2606.
- Zhu, Y., Liu, T.W., Madden, Z., Yuzwa, S.A., Murray, K., Cecioni, S., Zachara, N., and Vocadlo, D.J. (2016). Post-translational O-GlcNAcylation is essential for nuclear pore integrity and maintenance of the pore selectivity filter. *J. Mol. Cell Biol.* 8, 2–16.

STAR★METHODS

KEY RESOURCES TABLE

REAGENT or RESOURCE	SOURCE	IDENTIFIER
Antibodies		
Rabbit Anti-Nup50	Abcam	Cat#ab137092
Rabbit Anti-Nup153	Abcam	Cat#ab84872; RRID: AB_1859766
Mouse Anti-TPR	Santa Cruz Biotechnology	Cat#sc-271565; RRID: AB_10649043
Rabbit Anti-Nup54	Abcam	Cat#ab220890
Mouse Anti-NUPL1	Abcam	Cat#ab69954; RRID: AB_1269611
Rat Anti-Nup62	Millipore	Cat#MABE1043
Rat Anti-Nup98	Abcam	Cat#ab50610; RRID: AB_881769
Rabbit Anti-GP210	Abcam	Cat#ab15601; RRID: AB_2236461
Rabbit Anti-TMEM48	Thermo Fisher Scientific	Cat#PA5-67130; RRID: AB_2664610
Rabbit Anti-TMEM48	Novus Biologicals	Cat#NBP1-91604; RRID: AB_11042869
Rabbit Anti-TMEM48	Novus Biologicals	Cat#NBP1-91603; RRID: AB_11030742
Rabbit Anti-POM121	Thermo Fisher Scientific	Cat#PA5-36498; RRID: AB_2553555
Rabbit Anti-POM121	Novus Biologicals	Cat#NBP2-19890
Mouse Anti-Nup93	Santa Cruz Biotechnology	Cat#sc-374399; RRID: AB_10990113
Rabbit Anti-Nup155	Abcam	Cat#ab199528
Rabbit Anti-Nup188	Thermo Fisher Scientific	Cat#PA5-63984; RRID: AB_2644894
Mouse Anti-Nup205	Santa Cruz Biotechnology	Cat#sc-377047
Rabbit Anti-AHCTF1	Thermo Fisher Scientific	Cat#PA5-56812; RRID: AB_2637780
Rabbit Anti-Nup37	Thermo Fisher Scientific	Cat#PA5-66007; RRID: AB_2664134
Rabbit Anti-Nup43	Abcam	Cat#ab69447; RRID: AB_1269608
Mouse Anti-Nup107	Thermo Fisher Scientific	Cat#MA110031; RRID: AB_2154446
Mouse Anti-Nup133	Santa Cruz Biotechnology	Cat#sc-376699; RRID: AB_11149388
Rabbit Anti-Nup133	Abcam	Cat#ab155990
Rabbit Anti-Nup160	Abcam	Cat#ab74147; RRID: AB_1524055
Rabbit Anti-Nup88	Abcam	Cat#ab79785; RRID: AB_2042496
Rabbit Anti-Nup214	Bethyl Laboratories	Cat#A300-716A; RRID: AB_533409
Mouse Anti-RANBP2	Santa Cruz Biotechnology	Cat#sc-74518; RRID: AB_2176784
Mouse Anti-414	Abcam	Cat#ab50008; RRID: AB_881761
Chicken Anti-NeuN	Millipore	Cat#ABN91; RRID: AB_11205760
Chicken Anti-GFP	Millipore	Cat#AB16901; RRID: AB_90890
Mouse Anti-TurboGFP	Origene Technologies	Cat#TA150041; RRID: AB_2622256
Rabbit Anti-TurboGFP	Thermo Fisher Scientific	Cat#PA5-22688; RRID: AB_2540616
Rabbit Anti-TDP-43	ProteinTech	Cat#10782-2-AP; RRID: AB_615042
Guinea Pig Anti-Map2	Synaptic Systems	Cat#188004; RRID: AB_2138181
Mouse Anti-Ran	BD Biosciences	Cat#610341; RRID: AB_397731
Mouse Anti-SMI32	Covance	Cat#SMI-32P; RRID: AB_2314912
Mouse Anti-Tuj1	Sigma Aldrich	Cat#MAB1637; RRID: AB_2210524
Rat Anti-NKX6.1	DSHB	Cat#F55A12; RRID: AB_532379
Goat Anti-Islet1	R&D Systems	Cat#AF1837; RRID: AB_2126324
Goat Anti-Olig2	R&D Systems	Cat#AF2418; RRID: AB_2157554
Rabbit Anti-C9ORF72	ProteinTech	Cat#22637-1-AP; RRID: AB_10953528
Mouse Anti-GAPDH	Life Technologies	Cat#AM4300; RRID: AB_2536381
Rabbit Anti-Alpha Tubulin	Cell Signaling	Cat#2125; RRID: AB_2619646

(Continued on next page)

Continued

REAGENT or RESOURCE	SOURCE	IDENTIFIER
Mouse Anti-DIG	Jackson Immunoresearch	Cat#200-002-156; RRID: AB_2339005
Goat Anti-Mouse Alexa 488	Invitrogen	Cat#A11029; RRID: AB_138404
Goat Anti-Rabbit Alexa 488	Invitrogen	Cat#A11034; RRID: AB_2576217
Goat Anti-Rat Alexa 488	Invitrogen	Cat#A11006; RRID: AB_2534074
Goat Anti-Chicken Alexa 488	Invitrogen	Cat#A11039; RRID: AB_142924
Goat Anti-Mouse Alexa 568	Invitrogen	Cat#A11031; RRID: AB_144696
Goat Anti-Rabbit Alexa 568	Invitrogen	Cat#A11036; RRID: AB_143011
Goat Anti-Rat Alexa 568	Invitrogen	Cat#A11077; RRID: AB_141874
Goat Anti-Guinea Pig Alexa 568	Invitrogen	Cat#A11075; RRID: AB_141954
Goat Anti-Mouse Alexa 647	Invitrogen	Cat#A21236; RRID: AB_141725
Goat Anti-Rabbit Alexa 647	Invitrogen	Cat#A21245; RRID: AB_141775
Goat Anti-Rat Alexa 647	Invitrogen	Cat#A21247; RRID: AB_141778
Goat Anti-Chicken Alexa 647	Invitrogen	Cat#A21449; RRID: AB_1500594
Goat Anti-Guinea Pig Alexa 647	Invitrogen	Cat#A21450; RRID: AB_141882
Donkey Anti-Mouse Alexa 488	Invitrogen	Cat#A21202; RRID: AB_141607
Donkey Anti-Rat Alexa 488	Invitrogen	Cat#A21208; RRID: AB_141709
Donkey Anti-Mouse Alexa 568	Invitrogen	Cat#A10037; RRID: AB_2534013
Donkey Anti-Goat Alexa 568	Invitrogen	Cat#A11057; RRID: AB_142581
Donkey Anti-Rabbit IgG HRP	Thermo Fisher Scientific	Cat#45-000-682
Horse Anti-Mouse IgG HRP	Cell Signaling	Cat#7076S; RRID: AB_330924
Mouse IgG Isotype Control	Thermo Fisher Scientific	Cat#02-610-0; RRID: AB_2532935
Rabbit IgG Isotype Control	Thermo Fisher Scientific	Cat#02-610-2; RRID: AB_2532938
Biological Samples		
Non-neurological control and C9orf72 postmortem tissue	Target ALS Human Postmortem Tissue Core	N/A
C9orf72 postmortem tissue	Emory University ADRC Tissue Bank	N/A
Chemicals, Peptides, and Recombinant Proteins		
LDN193189	Stemgent	Cat#04-0074-02
SB431542	STEMCELL Technologies	Cat#72234
CHIR99021	Sigma-Aldrich	Cat#SML1046
Retinoic Acid	Sigma-Aldrich	Cat#R2625
SAG	Cayman Chemicals	Cat#11914
Compound E	Millipore	Cat#565790
DAPT	Sigma-Aldrich	Cat#D5942
db-cAMP	Millipore	Cat#28745
Ascorbic Acid	Sigma-Aldrich	Cat#A4544
BDNF	PeproTech	Cat#450-02
GDNF	PeproTech	Cat#450-10
L-glutamic acid	Sigma Aldrich	Cat#G1251
Propidium Iodide	Thermo Fisher Scientific	Cat#P3566
Dextran, Texas Red, 70,000 MW	Thermo Fisher Scientific	Cat#D1864
Fluorescein isothiocyanate dextran, 500,000 MW	Sigma-Aldrich	Cat#FD500S
DTT	Sigma-Aldrich	Cat#D0632
Actinomycin D	Sigma-Aldrich	Cat#A9415
Cycloheximide	Sigma-Aldrich	Cat#C7698
Protease Inhibitor Cocktail Set III, EDTA-free	Millipore	Cat#539134
Complete Mini EDTA-free Protease Inhibitor Cocktail	Roche	Cat#11836170001
TurboDNase	Thermo Fisher Scientific	Cat#AM2238

(Continued on next page)

Continued

REAGENT or RESOURCE	SOURCE	IDENTIFIER
RNaseOUT	Thermo Fisher Scientific	Cat#10777019
RNase A	Thermo Fisher Scientific	Cat#EN0531
Bovine Serum Albumin Fraction V	Sigma Aldrich	Cat#3117057001
Ribonucleoside-Vanadyl Complex	New England BioLabs	Cat#S1402S
Salmon Sperm DNA	Thermo Fisher Scientific	Cat#15-632-011
E.coli tRNA	Millipore	Cat#10109541001
Critical Commercial Assays		
Autofluorescence Eliminator Reagent	Millipore	Cat#2160
P3 Primary Cell 4D Nucleofector Kit	Lonza	Cat#V4XP-3024
Nuclei PURE Prep Nuclei Isolation Kit	Sigma-Aldrich	Cat#NUC201
Streptavidin Coated Plates	Meso Scale Discovery	Cat#L45SA-2
SuperSignal West Pico PLUS ECL Kit	Thermo Fisher Scientific	Cat#34580
Immonilon ECL Ultra Western HRP Substrate	Millipore	Cat#WBULS0100
BLOT-FASTSTAIN	G Biosciences	Cat#786-34
RNAeasy Mini Kit	QIAGEN	Cat#74104
Ambion TRIzol Reagent	Thermo Fisher Scientific	Cat#15-596-018
SuperScript IV First-Strand Synthesis System	Thermo Fisher Scientific	Cat#18091050
High-Capacity cDNA Reverse Transcription Kit	Thermo Fisher Scientific	Cat#4368814
TaqMan Fast Advanced Master Mix	Thermo Fisher Scientific	Cat#44-449-64
Experimental Models: Cell Lines		
Human iPSC: EDi036-A	Cedars-Sinai Induced Pluripotent Stem Cell Core	https://biomanufacturing.cedars-sinai.org/product/cs0594ictr-lbcnxx/
Human iPSC: EDi037-A	Cedars-Sinai Induced Pluripotent Stem Cell Core	https://biomanufacturing.cedars-sinai.org/product/cs0702ictr-lbcnxx/
Human iPSC: EDi029-A	Cedars-Sinai Induced Pluripotent Stem Cell Core	https://biomanufacturing.cedars-sinai.org/product/cs0188ictr-lbcnxx/
Human iPSC: EDi034-A	Cedars-Sinai Induced Pluripotent Stem Cell Core	https://biomanufacturing.cedars-sinai.org/product/cs0465ictr-lbcnxx/
Human iPSC: EDi022-A	Cedars-Sinai Induced Pluripotent Stem Cell Core	https://biomanufacturing.cedars-sinai.org/product/cs0617ictr-lbcnxx/
Human iPSC: EDi044-A	Cedars-Sinai Induced Pluripotent Stem Cell Core	https://biomanufacturing.cedars-sinai.org/product/cs1185ictr-lbcnxx/
Human iPSC: CS1ATZ	Cedars-Sinai Induced Pluripotent Stem Cell Core	https://biomanufacturing.cedars-sinai.org/product/cs1atzictr-nxx/
Human iPSC: CS8PAA	Cedars-Sinai Induced Pluripotent Stem Cell Core	https://biomanufacturing.cedars-sinai.org/product/cs8paaictr-nxx/
Human iPSC: EDi043-A	Cedars-Sinai Induced Pluripotent Stem Cell Core	https://biomanufacturing.cedars-sinai.org/product/cs1050ictr-lbcnxx/
Human iPSC: CS0201	Cedars-Sinai Induced Pluripotent Stem Cell Core	https://biomanufacturing.cedars-sinai.org/product/cs0201ictr-nxx/
Human iPSC: CS0002	Cedars-Sinai Induced Pluripotent Stem Cell Core	https://biomanufacturing.cedars-sinai.org/product/cs0002ictr-nxx/
Human iPSC: CS9XH7	Cedars-Sinai Induced Pluripotent Stem Cell Core	https://biomanufacturing.cedars-sinai.org/product/cs9xh7ictr-nxx/
Human iPSC: CS0BUU	Cedars-Sinai Induced Pluripotent Stem Cell Core	https://biomanufacturing.cedars-sinai.org/product/cs0buuials-nxx/
Human iPSC: CS7VCZ	Cedars-Sinai Induced Pluripotent Stem Cell Core	https://biomanufacturing.cedars-sinai.org/product/cs7vczials-nxx/
Human iPSC: CS0LPK	Cedars-Sinai Induced Pluripotent Stem Cell Core	https://biomanufacturing.cedars-sinai.org/product/cs0lpkials-nxx/

(Continued on next page)

Continued

REAGENT or RESOURCE	SOURCE	IDENTIFIER
Human iPSC: CS6ZLD	Cedars-Sinai Induced Pluripotent Stem Cell Core	https://biomanufacturing.cedars-sinai.org/product/cs6zldials-nxx/
Human iPSC: CS8KT3	Cedars-Sinai Induced Pluripotent Stem Cell Core	https://biomanufacturing.cedars-sinai.org/product/cs8kt3ials-nxx/
Human iPSC: CS2YNL	Cedars-Sinai Induced Pluripotent Stem Cell Core	https://biomanufacturing.cedars-sinai.org/product/cs2ynlials-nxx/
Human iPSC: CS0NKC	Cedars-Sinai Induced Pluripotent Stem Cell Core	https://biomanufacturing.cedars-sinai.org/product/cs0nkcials-nxx/
Human iPSC: CS6CLW	Cedars-Sinai Induced Pluripotent Stem Cell Core	https://biomanufacturing.cedars-sinai.org/product/cs6clwials-nxx/
Human iPSC: 59-1	Ababneh et al., 2020	N/A
Human iPSC: OXC9-02-02	Dafinca et al., 2016	N/A
Human iPSC: 3231	Justin Ichida	N/A
Human iPSC: 3-11	Justin Ichida	N/A
Primary Human Astrocytes	ScienCell	Cat#1800-5
HEK293T Cells	ATCC	Cat#CRL-11268; RRID: CVCL_1926
Oligonucleotides		
C9orf72 and Scrambled ASOs	Ionis Pharmaceuticals	N/A
C9orf72 Primers	Lagier-Tourenne et al., 2013 ; This Paper (Table S2)	N/A
DIG G ₄ C ₂ FISH probe	QIAGEN	N/A
DIG scrambled FISH probe	QIAGEN	N/A
Nup50 TaqMan Gene Expression Assay	Thermo Fisher Scientific	Cat#Hs00855432_g1
TPR TaqMan Gene Expression Assay	Thermo Fisher Scientific	Cat#Hs00162918_m1
Nup98 TaqMan Gene Expression Assay	Thermo Fisher Scientific	Cat#Hs00180522_m1
GP210 TaqMan Gene Expression Assay	Thermo Fisher Scientific	Cat#Hs00227779_m1
NDC1 TaqMan Gene Expression Assay	Thermo Fisher Scientific	Cat#Hs00917927_m1
POM121 TaqMan Gene Expression Assay	Thermo Fisher Scientific	Cat#Hs00208021_m1
Nup107 TaqMan Gene Expression Assay	Thermo Fisher Scientific	Cat#Hs00220703_m1
Nup133 TaqMan Gene Expression Assay	Thermo Fisher Scientific	Cat#Hs00217272_m1
Nup62 TaqMan Gene Expression Assay	Thermo Fisher Scientific	Cat#Hs02621445_s1
Nup205 TaqMan Gene Expression Assay	Thermo Fisher Scientific	Cat#Hs01046411_m1
GAPDH TaqMan Gene Expression Assay	Thermo Fisher Scientific	Cat#Hs02786624_g1
RPS18 TaqMan Gene Expression Assay	Thermo Fisher Scientific	Cat#Hs01375212_g1
18S rRNA TaqMan Gene Expression Assay	Thermo Fisher Scientific	Cat#Hs99999901_s1
Recombinant DNA		
Plasmid: pCMV6-AC-GFP-POM121	Origene Technologies	Cat#RG235113
Plasmid: pCMV6-AC-GFP-Nup133	Origene Technologies	Cat#RG204410
Plasmid: pCMV6-AC-GFP-Nup98	Origene Technologies	Cat#RG213664
Plasmid: pCMV6-AC-GFP-GP210	Origene Technologies	Cat#RG213658
Plasmid: pCMV6-AC-GFP-NDC1	Origene Technologies	Cat#RG200141
Plasmid: pEGFP-POM121	Eilenberg Lab; Doucet et al., 2010 ; Talamas and Hetzer, 2011 ; Franks et al., 2016	N/A
Plasmid: pQXCIB-sPOM121	Franks et al., 2016	N/A
Plasmid: pCMV6-AC-GFP-Trim21	Origene Technologies	Cat#RG202088
Plasmid: pLenti-NLS-tdTomato-NES	Zhang et al., 2015	RRID: Addgene_112579
Plasmid: pcDNA3.1-EGFP-(GA) ₅₀	Wen et al., 2014	N/A
Plasmid: pcDNA3.1-EGFP-(GR) ₅₀	Wen et al., 2014	N/A

(Continued on next page)

Continued

REAGENT or RESOURCE	SOURCE	IDENTIFIER
Plasmid: pcDNA3.1-EGFP-(PR) ₅₀	Wen et al., 2014	N/A
Plasmid: pcDNA3.1+ 36RO	Mizielinska et al., 2014	N/A
Plasmid: pcDNA3.1+ 106RO	Mizielinska et al., 2014	N/A
Plasmid: pcDNA3.1+ 288 RO	Mizielinska et al., 2014	N/A
Plasmid: 5' UTR CGG 99x FMR1-EGFP	Addgene	Cat#63091; RRID: Addgene_63091
Plasmid: pCTG202	Nutter et al., 2019; Osborne and Thornton, 2008	N/A
Plasmid: pCMV6-AC-GFP	Origene Technologies	Cat#PS100010
Plasmid: mEGFP-N1	Addgene	Cat#54767; RRID: Addgene_54767
Plasmid: pmaxGFP	Lonza	Cat#V4XP-3024
Software and Algorithms		
FIJI	NIH	https://fiji.sc ; RRID: SCR_002285
Imaris	Bitplane	https://imaris.oxinst.com ; RRID: SCR_007370
GraphPad Prism 7	GraphPad Software	https://www.graphpad.com ; RRID: SCR_002798
GraphPad Prism 8	GraphPad Software	https://www.graphpad.com ; RRID: SCR_002798
Zen 2 Pro	Carl Zeiss	https://www.zeiss.com/microscopy/us/products/microscope-software/zen.html ; RRID: SCR_013672
Zen 2.1	Carl Zeiss	https://www.zeiss.com/microscopy/us/products/microscope-software/zen.html ; RRID: SCR_013672
Zen 2.3 SP1	Carl Zeiss	https://www.zeiss.com/microscopy/us/products/microscope-software/zen.html ; RRID: SCR_018163
Other		
MTeSR	STEMCELL Technologies	Cat#85850
IMDM	Life Technologies	Cat#12440053
F12	Life Technologies	Cat#11765062
DMEM	Life Technologies	Cat#11995073
Penicillin Streptomycin	GIBCO	Cat#15140122
NEAA	Life Technologies	Cat#11140-050
B27	GIBCO	Cat#17504044
N2	Life Technologies	Cat#17502048
Versene	Thermo Fisher Scientific	Cat#15040066
ReLeSR	STEMCELL Technologies	Cat#05872
EZ Pass Tool	Life Technologies	Cat#23181-010
StemPro Accutase	GIBCO	Cat#A11105-01
Trypsin-EDTA	Life Technologies	Cat#25300054
Matrigel	Corning	Cat#354230
PureCol Type I Collagen Solution	Advanced BioMatrix	Cat#5005
ACSF	Tocris	Cat#3525
Normal Goat Serum	Vector Labs	Cat#S-1000; RRID: AB_2336615
Donkey Serum	Sigma-Aldrich	Cat#D9663; RRID: AB_2810235
ProLong Gold Antifade Reagent	Invitrogen	Cat#P36930
ProLong Gold Antifade Reagent with DAPI	Life Technologies	Cat#P36931
Hoescht	Thermo Fisher Scientific	Cat#H3570
DAKO Protein Block Serum-Free	Dako	Cat#X0909

(Continued on next page)

Continued

REAGENT or RESOURCE	SOURCE	IDENTIFIER
Antibody Diluent with Background-Reducing Components	Dako	Cat#S302283-2
OptiPrep Density Gradient Medium	Sigma-Aldrich	Cat#D1556
RIPA	Sigma Aldrich	Cat#R0278
NucBlue Live ReadyProbes	Thermo Fisher Scientific	Cat#R37605
Slide-A-Lyzer MINI Dialysis Device, 20K MWCO	Thermo Fisher Scientific	Cat#88402
Amicon Ultra-0.5 Centrifugal Filter Unit	Millipore	Cat#UFC510024
NanoDrop 1000 Spectrophotometer	Thermo Fisher Scientific	N/A
Applied Biosystems Step One Plus Real Time PCR Machine	Thermo Fisher Scientific	Cat#4376600
ImageQuant LAS 4000	GE Healthcare	N/A
MESO QuickPlex SQ 120	Meso Scale Discovery	N/A
CytoSpin 4	Thermo Fisher Scientific	Cat#A78300003
High Tolerance Coverslips	MatTek	Cat#PCS-170-1818
Zeiss ELYRA S1	Carl Zeiss	N/A
Zeiss LSM 800 with Airyscan	Carl Zeiss	RRID: SCR_015963
Zeiss Apotome	Carl Zeiss	N/A

RESOURCE AVAILABILITY

Lead Contact

Further information and requests for resources and reagents should be directed to and will be fulfilled by the Lead Contact, Jeffrey D Rothstein (jrothstein@jhmi.edu).

Materials Availability

This study did not generate new unique reagents.

Data and Code Availability

This study did not generate or analyze datasets or code.

EXPERIMENTAL MODEL AND SUBJECT DETAILS

iPSC Neuron Differentiation

Peripheral blood mononuclear cell (PBMC)-derived iPSC lines from C9orf72-ALS patients and non-neurological controls were obtained from the Cedars-Sinai Answer ALS repository (see [Table S1](#) for demographic information). Fibroblast derived isogenic iPSC lines were a kind gift from Kevin Talbot ([Ababneh et al., 2020](#)). The C9orf72 null line was a gift from Justin Ichida. While Nup alterations were reproducible across all C9orf72 iPSC lines evaluated, the influence of sex was not investigated in this study. iPSCs were maintained in MTeSR according to standard Cedars Sinai protocols and differentiated into spinal neurons according to the direct induced motor neurons (diMNs) protocol ([Figure S1A](#)), which generates a mixed population consisting of 20%–30% islet-1 positive motor neurons. Briefly, iPSC colonies were maintained on Matrigel coated 10 cm dishes for three weeks before passaging for differentiation. Once iPSC colonies reached 30%–40% confluence (about 4–5 days after passaging), stage 1 media consisting of 47.5% IMDM (GIBCO), 47.5% F12 (GIBCO), 1% NEAA (GIBCO), 1% Pen/Strep (GIBCO), 2% B27 (GIBCO), 1% N2 (GIBCO), 0.2 μM LDN193189 (Stemgent), 10 μM SB431542 (StemCell Technologies), and 3 μM CHIR99021 (Sigma Aldrich) was added and exchanged daily until day 6. On day 6 of differentiation, cells were incubated in StemPro Accutase (GIBCO) for 5 minutes at 37°C. Cells were collected from plates and centrifuged at 500 × g for 1.5 minutes. Cells were plated at 1 × 10⁶ cells per well of a 6 well plate or 5 × 10⁶ cells per T25 flask in stage 2 media consisting of 47.5% IMDM (GIBCO), 47.5% F12 (GIBCO), 1% NEAA (GIBCO), 1% Pen/Strep (GIBCO), 2% B27 (GIBCO), 1% N2 (GIBCO), 0.2 μM LDN193189 (Stemgent), 10 μM SB431542 (StemCell Technologies), 3 μM CHIR99021 (Sigma Aldrich), 0.1 μM all-trans RA (Sigma Aldrich), and 1 μM SAG (Cayman Chemicals). Media was exchanged daily until day 12. For the majority of experiments, on day 12 of differentiation, cells were switched to stage 3 media consisting of 47.5% IMDM (GIBCO), 47.5% F12 (GIBCO), 1% NEAA (GIBCO), 1% Pen/Strep (GIBCO), 2% B27 (GIBCO), 1% N2 (GIBCO), 0.1 μM Compound E (Millipore), 2.5 μM DAPT (Sigma Aldrich), 0.1 μM db-cAMP (Millipore), 0.5 μM all-trans RA (Sigma Aldrich), 0.1 μM SAG (Cayman Chemicals), 200 ng/mL Ascorbic Acid (Sigma Aldrich), 10 ng/mL BDNF (PeproTech), 10 ng/mL GDNF (PeproTech). For all whole cell imaging (TDP-43, Ran), cells were trypsinized and plated in 24 well optical bottom plates (Cellvis) at a

density of 250,000 cells per well. Stage 3 media was exchanged every 3 days for the duration of the experiment. All cells were maintained at 37°C with 5% CO₂ until day 18, 32, or 46 of differentiation as indicated by each experiment. iPSCs and iPSNs routinely tested negative for mycoplasma.

Human Tissue Immunofluorescence

Postmortem paraffin embedded motor cortex (See [Table S2](#) for demographic information) was rehydrated with xylene 3X 5 mins, 100% ethanol 2X 5 mins, 90% ethanol 5 mins, 70% ethanol, dH₂O 3X 5 mins. Antigen retrieval was performed using *Tissue-Tek* antigen retrieval solution (*IHC World*) for 1 hour in a steamer. Slides were cooled for 10 mins, washed 3X 5 mins with dH₂O followed by 2X 5 mins in 1X PBS. Tissue was permeabilized with 0.4% Triton X-100 in 1X PBS for 10 mins with gentle agitation on a shaker. Slides were washed 3X 5 mins with 1X PBS and blocked in DAKO protein-free serum block (DAKO) overnight in a humidified chamber at 4°C. Tissue was incubated in primary antibody diluted in DAKO antibody diluent reagent with background reducing components (DAKO) for 12 hours at room temperature with gentle agitation on a shaker followed by 2 days at 4°C (See [Table S5](#) for antibody information). Slides were washed 3X 5 mins in 1X PBS and incubated in secondary antibody diluted in DAKO antibody diluent reagent with background reducing components (DAKO) for 1 hour at room temperature with gentle agitation on a shaker (See [Table S5](#) for antibody information). Slides were washed 3X 5 mins in 1X PBS, rinsed briefly with autofluorescence eliminator reagent (Millipore), washed 5X 5 mins in 1X PBS, stained with Hoescht diluted 1:1000 in 1X PBS for 20 mins, and washed 3X 5 mins in 1X PBS. Slides were coverslipped using Prolong Gold Antifade Reagent with DAPI and nuclei from Map2 positive Layer V neurons were imaged with a Zeiss Axioimager Z2 fluorescent microscope equipped with an apotome2 module. POM121 nuclear intensity was quantified using FIJI. While POM121 alterations were reproducible across all C9orf72 ALS patients, the influence of sex was not investigated in this study. Images presented are maximum intensity projections generated in Zeiss Zen Blue 2.3.

METHOD DETAILS

ASO Treatment of iPSC Derived Neurons

Scrambled ASO (676630): CCTATAGGACTATCCAGGAA and G₄C₂ ASO (619251): CAGGCTGCGGTTGTTCCCT were provided by Ionis Pharmaceuticals. For 5 day ASO treatment, 5 μM scrambled or sense targeting ASO was added to the culture media on day 30. Media was exchanged and ASO replaced on day 32 and experiments were conducted on day 35 of differentiation.

RT-qPCR

Samples were harvested in 1x DPBS with calcium and magnesium, then spun down in a microcentrifuge and the DPBS was aspirated. RLT Buffer (500 μL) was added to samples and RNA was isolated with an *RNAeasy* kit (QIAGEN). RNA concentrations were determined using a NanoDrop 1000 spectrophotometer (Thermo Fisher Scientific). For C9orf72 detection, 1 μg RNA was used for cDNA synthesis using gene specific primers and a Superscript IV First-Strand cDNA Synthesis System (Thermo Fisher Scientific). RT-qPCR reactions were carried out using TaqMan Gene Expression Master Mix (TaqMan) and an Applied Biosystems Step One Plus Real Time PCR Machine (Applied Biosystems) using previously described primer/probe sets (see [Table S3](#) for sequences) ([Lagier-Tourenne et al., 2013](#)). Levels of C9orf72 transcripts were normalized to GAPDH. For Nup mRNA detection, 1 μg RNA was used for cDNA synthesis using random hexamers and a Superscript IV First-Strand cDNA Synthesis System (Thermo Fisher Scientific). RT-qPCR reactions were carried out using TaqMan Gene Expression Master Mix (TaqMan) and an Applied Biosystems Step One Plus Real Time PCR Machine (Applied Biosystems) using TaqMan Gene Expression Assays (see [Table S4](#)) Levels of Nup transcripts were normalized to GAPDH.

Actinomycin D Treatment

On day 32 of differentiation, control and C9orf72 iPSNs were incubated with 10 μg/mL Actinomycin D. Samples were harvested following 0.5, 1, 2, 3.5, and 5 hour incubation with Actinomycin D. RNA was isolated using standard TRIzol-LS (Thermo Fisher Scientific) phenol-chloroform extraction and 1 μg RNA was used for cDNA synthesis using a high-capacity cDNA reverse transcription kit (Thermo Fisher Scientific). RT-qPCR was performed as described above. Nup mRNA was normalized to RPS18.

Polyribosome Fractionation

On day 32 of differentiation, iPSNs were incubated with 100 μg/mL cycloheximide for 5 minutes. iPSNs were subsequently washed with ice cold 1X DPBS containing 100 100 μg/mL cycloheximide and harvested with a cell scraper. iPSNs were pelleted by centrifugation at 500 x g for 5 min and washed with ice cold 1X DPBS supplemented with 100 μg/mL cycloheximide. Following pelleting by centrifugation, DPBS was aspirated and iPSNs were lysed in 400 μL ice cold polysome lysis buffer (20 mM Tris-HCl pH 7.4, 150 mM NaCl, 5 mM MgCl₂, 1% Triton X-100, 1X protease inhibitor cocktail set III, EDTA-free (Millipore), 100 μg/mL cycloheximide, 1 mM DTT, 25 U/ml TurboDNase, 20 U/ml RNase inhibitor (RNaseOUT, Thermo Fisher Scientific) by trituration through a 27-gauge needle 6-8 times. Lysates were snap frozen in liquid nitrogen and stored at -80°C until use. Lysates were clarified by centrifugation at 15,000 x g at 4°C for 5 min. 50 μL lysate was reserved for inputs and 350 μL lysate used for fractionation. For fractionation, a 10%-50% (w/v) sucrose gradient was prepared in a polysome buffer (20 mM Tris-HCl pH 7.4, 150 mM NaCl, 5 mM MgCl₂, 1X protease inhibitor cocktail, cycloheximide 100 μg/ml, 1 mM DTT, and 20 U/ml RNaseOUT. 350 μL lysate were loaded on the sucrose

gradient and centrifuged at 35,000 × g with a Beckman SW41 rotor at 4°C for 3 h. Fractions were collected from the top and UV absorbance monitored using a Gradient Station (BioCamp) equipped with ECONO UV monitor (BioRad). 500 µl fraction were collected using a FC203B (Gilon) fraction collector. RNA was isolated using TRIzol-LS (Thermo Fisher Scientific) and standard phenol-chloroform extraction. cDNA synthesis was performed using a high-capacity cDNA reverse transcription kit (Thermo Fisher Scientific). RT-qPCR was performed as described above. Nup mRNA in each fraction was normalized to 18S rRNA.

Meso Scale Discovery (MSD) ELISA

All reagents were purchased from MSD unless otherwise noted. 96-well small spot streptavidin coated plates were blocked overnight at 4° in 1% blocker A in PBS. Wells were washed 3X in PBS-0.05% Tween (PBST) and then coated with 0.35 µg/mL biotinylated rabbit anti-GP antibody (Cheng et al., 2019) for 1 hour at room temperature. Following 3 washes with PBST, cell lysates were added to wells in duplicate. A standard curve of GP₈ peptide was included on each plate. Plates were incubated for 2 hours at room temperature, wells were washed three times with PBST, and incubated with 0.25 µg/mL sulfo-tagged detection antibody (Cheng et al., 2019) for 1 hour. Wells were washed 3X with PBST and 150 µL read buffer was added. Samples were immediately imaged using MESO Quick-Plex SQ 120. Specificity was verified using lysates of HEK cells overexpressing GFP-tagged dipeptide repeat proteins. Linearity across range of interest assessed by serial dilution.

Western Blots

Samples were harvested in 1x PBS, then spun down in a microcentrifuge and the PBS was aspirated. Samples were resuspended in RIPA buffer (Millipore Sigma) containing 1x protease inhibitor cocktail (Roche). Samples were spun at 12,000 g for 15 minutes to remove debris, and the supernatant was transferred to a new tube. 6x Laemmli buffer (12% SDS, 50% glycerol, 3% Tris-HCl pH 7.0, 10% 2-mercaptoethanol in dH₂O, bromophenol blue to color) was added to a final 1x concentration. Equal protein (by mass for quantifiable samples, by volume for unquantifiable samples) was loaded into 4%–20% acrylamide gels and run until the dye front reached the bottom. Protein was transferred onto nitrocellulose membrane (Bio-Rad). Following transfer, blots were blocked for 1 hour in 5% milk in 1x TBS-Triton (0.1%). Blots were probed with primary antibody (see Table S5) overnight (approximately 16 hours) at 4 degrees. Blots were washed four times in 1x TBST for 10 minutes each, probed with secondary antibody for 1 hour at room temperature, and washed another four times in 1x TBST for 10 minutes each. ECL substrate (Millipore Sigma, Thermo Fisher Scientific) was applied for 30 s, then images were taken using the GE Healthcare ImageQuant LAS 4000. Images were quantified using FIJI. For nuclei westerns, nucleoporins were normalized to total protein levels using the BLOT-FastStain Kit (G-Biosciences). For Trim Away westerns, GAPDH was used for normalization.

Nuclei Isolation and Super Resolution Structured Illumination Microscopy

Nuclei were isolated using Nuclei Pure Prep Nuclei Isolation Kit (Sigma Aldrich) using a 1.85 M sucrose gradient to enrich for neuronal nuclei. A 1.8 M gradient was used for astrocyte and HEK293T nuclei and a 1.9 M gradient was used for oligodendrocyte nuclei. For preparation of iPSN, astrocyte, or HEK293T lysates, media was aspirated from each well and cells were briefly rinsed with 1X PBS. iPSNs were scraped in lysis buffer using a cell scraper, transferred to a 50 mL conical tube, and vortexed. For preparation of post-mortem human brain lysates, 75–100 mg of fresh frozen tissue was homogenized in lysis buffer using a dounce homogenizer. Sucrose gradients were assembled and centrifuged following the Nuclei Pure Prep Nuclei Isolation Kit protocol (Sigma Aldrich). Samples were centrifuged at 15,600 rpm and 4°C using a Swi32T swinging bucket rotor and Beckman ultracentrifuge (Beckman Coulter) for 45 minutes. Following isolation, nuclei were resuspended in 1 mL of Nuclei Storage Buffer and 25–100 µL was spun onto slides coated with 1 mg/mL collagen (Advanced Biomatrix) using a CytoSpin 4 Centrifuge (Thermo Fisher Scientific). Nuclei were fixed in 4% PFA for 5 minutes, washed with 1X PBS 3X 10 minutes, permeabilized with 1X PBST containing 0.1% Triton X-100 for 15 minutes, blocked in 10% normal goat serum diluted in 1X PBS for 1 hour, and incubated in primary antibody overnight at 4°C (See Table S5 for antibody information). The next day, nuclei were washed with 1X PBS 3X 10 minutes, incubated in secondary antibody (See Table S5 for antibody information) for 1 hour at room temperature, and washed in 1X PBS 3X 10 minutes. Nuclei were coverslipped using Prolong Gold Antifade Reagent (Invitrogen) and 18 mm x 18 mm 1.5 high tolerance coverslips (MatTek). NeuN or GFP positive nuclei were identified looking through microscope eyepieces and a single z slice image (~110 nm thick) was acquired with widefield imaging on a Zeiss ELYRA S1. Only the Nup channel(s) subsequently imaged by super resolution structured illumination microscopy (SIM) with 5 grid rotations and optimal z sectioning using a Zeiss ELYRA S1. SIM images were constructed using default parameters with Zeiss Zen Black 2.3 SP1 software as per Zeiss recommendation. Each image acquired contained an individual NeuN or GFP positive nucleus to allow for the most accurate processing and 3D reconstruction. All images for a given Nup were imaged and acquired with identical parameters. Nucleoporin spots and volume quantification was automated using Imaris version 9.2.0 (Bitplane) and the 3D suite in FIJI 1.52i and 1.52p as previously described (Eftekharzadeh et al., 2018). Briefly, nucleoporin spots were counted using automated spot detection in which a Bayesian classifier which takes into account features such as volume, average intensity, and contrast was applied to detect and segment individual spots. The total number of nucleoporin spots was determined using a 3D rendering of super resolution SIM images where z-slices were taken through the entire nucleus. When individual nucleoporin spots could not be resolved due to limits of resolution of immunofluorescent SIM, the percent total nuclear volume occupied by the nucleoporin was calculated. X and y axis length was measured in the center z-slice for each nucleus and Z axis length was estimated by multiplying z-slice thickness by the number of z slices imaged for each nucleus. These measurements were used to calculate total

nuclear volume. For volume of the nucleoporin, automatic thresholding was applied and 3D suite in FIJI was used to determine the volume of the thresholded area for each nucleus. Nucleoporin volume was divided by total nuclear volume to yield a percentage of the total nuclear volume occupied by a given nucleoporin. In total across all experiments, over 1,000,000 nuclei were imaged and analyzed. Images presented are 3D maximum intensity projections generated in Zeiss Zen Black 2.3 SP1. With the exception [Figure 6C](#), nucleoporin images were faux colored green for contrast and display purposes.

Immunofluorescent Staining and Confocal Imaging

On day 12 of differentiation, iPSNs were plated in 24 well optical bottom plates (Cellvis). iPSNs were fixed in 4% PFA for 15 minutes, washed with 1X PBS 3X 10 minutes, permeabilized with 1X PBST containing 0.3% Triton X-100 for 15 minutes, blocked in 10% normal goat serum diluted in 1X PBS for 1 hour, and incubated in primary antibody for 2 hours at room temperature (See [Table S5](#) for antibody information). iPSNs were then washed with 1X PBS 3X 10 minutes, incubated in secondary antibody (See [Table S5](#) for antibody information) for 1 hour at room temperature, washed in 1X PBS 2X 10 minutes, incubated with Hoescht diluted 1:1000 in 1X PBS for 10 minutes, and washed in 1X PBS 2X 10 minutes. iPSNs were mounted using Prolong Gold Antifade Reagent with DAPI. iPSNs were imaged using a Zeiss LSM 800 confocal microscope and nuclear intensity and N/C ratios were calculated with FIJI as previously described ([Zhang et al., 2015](#)). Images presented are maximum intensity projections generated in Zeiss Zen Blue 2.3.

Plasmids and Nucleofection for Nup, G₄C₂ repeat RNA, and DPR Overexpression

iPSNs were dissociated with accutase and transfected in suspension using the Lonza nucleofection system (program DC104) and a Lonza P3 Primary Cell 4D Nucleofector Kit (Lonza). GFP tagged POM121, Nup133, NDC1, GP210, and Nup98 plasmids were obtained from Origene Technologies. Additional GFP tagged POM121 and sPOM121 plasmids ([Franks et al., 2016](#)) were a kind gift from Martin Hetzer. GFP control plasmids were obtained from Origene Technologies, Addgene, and Lonza. GFP tagged Poly(GA)₅₀, Poly(GR)₅₀, and Poly(PR)₅₀ DPR plasmids ([Wen et al., 2014](#)) were a kind gift from Davide Trott and (G₄C₂)_n RNA only plasmids ([Mizielinska et al., 2014](#)) were a kind gift from Adrian Isaacs. The (CGG)₉₉ plasmid was obtained from Addgene and the (CTG)₂₀₂ plasmid ([Nutter et al., 2019; Osborne and Thornton, 2008](#)) was a kind gift from Maurice Swanson. For Nup overexpression experiments, 5 × 10⁶ iPSNs were nucleofected with 4 µg of DNA on day 30 of differentiation. Expression was observed at day 31 and iPSNs were assayed at day 46 of differentiation. For DPR overexpression experiments, 5 × 10⁶ iPSNs were nucleofected with 4 µg or 1 µg of DNA on day 18 and assayed at day 20 or 25 of differentiation respectively. For RNA only experiments, 5 × 10⁶ iPSNs were nucleofected with 4 µg or 1 µg of DNA on day 18 and assayed at day 20 or 25 of differentiation respectively. For CGG and CTG overexpression experiments, 5 × 10⁶ iPSNs were nucleofected with 1 µg of DNA on day 18 and assayed at day 25 of differentiation. Following nucleofection of all overexpression plasmids, media was exchanged every 48 hours until iPSNs were assayed unless otherwise noted.

Knockdown of Nups by Trim Away

Trim21 mediated knockdown of Nups was modified from a previously described protocol ([Clift et al., 2017](#)). POM121 (Thermo Fisher Scientific), Nup133 (Santa Cruz Biotechnology), NDC1 (Novus Biologicals), and GAPDH (Cell Signaling) antibodies were dialyzed using Slide-A-Lyzer MINI Dialysis Device, 20K MWCO (Thermo Fisher Scientific). Following dialysis, antibodies were concentrated using Amicon Ultra-0.5 Centrifugal Filter Unit with Ultracel-100 membrane (Millipore). Antibody concentration was determined using a NanoDrop 1000 spectrophotometer (Thermo Fisher Scientific) as described ([Clift et al., 2017](#)). On day 18 of differentiation, 5 × 10⁶ iPSNs were nucleofected with 5 µg of antibody and 4 µg Trim21 GFP plasmid DNA (Origene Technologies) with Lonza P3 Primary Cell 4D Nucleofector Kit (Lonza) using program DC154. The next day, Trim21 GFP expression was observed and iPSNs were assayed on day 20 of differentiation.

NLS-tdTomato-NES (S-tdTomato) Nucleocytoplasmic Transport Assay

On day 32 of differentiation, control and C9orf72 iPSNs were nucleofected using the Lonza nucleofection system (program DC104) and a Lonza P3 Primary Cell 4D Nucleofector Kit (Lonza) as described above. One day later, on day 33 of differentiation, iPSNs were transduced with NLS-tdTomato-NES (S-tdTomato) lenti virus as previously described ([Zhang et al., 2015](#)). On days 34, 36, and 43 of differentiation (1, 3, and 10 or 2, 5, and 11 days post S-tdTomato transduction or POM121 OE respectively), iPSNs were fixed with 4% PFA for 15 mins, washed 3X 10 mins with 1X PBS and then incubated with Hoescht diluted 1:1000 in 1X PBS for 10 minutes, and washed in 1X PBS 2X 10 minutes. iPSNs were then immediately imaged using a Zeiss LSM 800 confocal microscope and the N/C ratio of S-tdTomato was calculated with FIJI as previously described ([Zhang et al., 2015](#)).

Glutamate Toxicity

On day 12 of differentiation, iPSNs were plated in 24 well optical bottom plates (Cellvis) at a density of 250,000 neurons per well. Neurons were rinsed with 1X PBS and fed with fresh stage 3 media daily remove dead cells and debris prior to incubation with glutamate. For POM121 overexpression experiments, iPSNs were split using accutase to dissociate cells and help promote single cell suspension, transfected as described above, and plated into optical bottom plates on day 30 of differentiation. For these experiments, iPSNs were washed with 1X PBS/fed daily from day 32–46 before the toxicity experiments were performed. Daily washes were performed to remove cells that died as a result of passage and nucleofection stress thus ensuring that on the day of the

experiment, we were only imaging PI incorporation in cells that died as a result of glutamate exposure. As a result of accumulated death over the 2 week period post-nucleofection, we note that the cells remaining on the day of the toxicity experiment are only a subset of the initial population dissociated and nucleofected. For a schematic representation of this experimental paradigm please see the flow chart ([Figure S24](#)) contained within the experimental procedures. For 5 day ASO treatment experiments, iPSNs were treated with 5 μ M ASO on day 30 and 32 during which time they were washed with 1X PBS. For G₄C₂ Repeat RNA only experiments, iPSNs were split and transfected with 1 μ g of DNA on day 18 as described above. iPSNs were washed/fed daily from day 19-25 before the toxicity experiments were performed. On the day of the experiment (day 46 for POM121 OE, day 35 for 5 Day ASO, day 25 for G₄C₂ Repeat RNA only), iPSNs were washed with 1X PBS to remove any remaining debris and dead cells. Media was replaced with ACSF (Tocris) containing 0, 1, 10, or 100 μ M glutamate (Sigma Aldrich). iPSNs were incubated at 37°C with 5% CO₂ for 4 hours. After 3.5 hours, one drop of NucBlue Live ReadyProbes (Thermo Fisher Scientific) and 1 μ M propidium iodide (Thermo Fisher Scientific) and returned to the incubator for 30 mins. iPSNs were imaged in an environmentally controlled chamber with a Zeiss LSM 800 confocal microscope. 10 images were taken and analyzed per well. PI and DAPI spots were counted using FIJI. For POM121 overexpression experiments, following live imaging, PI and NucBlue were washed out of neurons and iPSNs were subsequently immunostained for GFP and Map2 as described above and imaged with a Zeiss LSM 800 confocal microscope.

Scanning Electron Microscopy

Previously published protocols ([Fichtman et al., 2014, 2019](#)) were modified to expose iPSN nuclei for high resolution imaging. Briefly, day 32 control and C9orf72 iPSNs were frozen in growth medium supplemented with 10% DMSO, shipped on dry ice, and stored under liquid nitrogen until use. Thawed cells were pelleted, resuspended in mildly hypotonic buffer in the absence of detergents, and gently passed through a 21-gauge needle. The specimens were then centrifuged onto the surface of 5 \times 5 mm² silicon chips (Ted Pella), fixed, and further processed for electron microscopy as previously described ([Fichtman et al., 2014, 2019](#)), including controlled dehydration through a graded series of ethanol solutions and critical-point drying on a K850 apparatus (Quorum Technologies). The specimens were then coated with a ~1 nm thick layer of iridium using a Q150T turbo-pumped sputter coater (Quorum Technologies) and imaged on a *Merlin* field emission scanning electron microscope (Zeiss) equipped with a secondary electron in-lens detector.

Dextran Exclusion

On day 32 of differentiation, iPSNs were rinsed briefly with 1X PBS to remove remaining traces of media. iPSNs were permeabilized in permeabilization buffer (10 mM Tris pH 7.5, 10% OptiPrep, ultrapure water) containing 200 μ g/mL digitonin on ice for 5 mins. iPSNs were then rinsed with ice cold transport buffer (4 mM HEPES-KOH pH 7.5, 22 mM KOAc, 0.4 mM Mg(OAc)₂, 1 mM NaOAc, 0.1 mM EGTA, 50 mM sucrose) 2X 5 mins. Permeabilized iPSNs were incubated with 0.6 mg/mL fluorescent dextrans diluted in transport buffer for 25 mins at room temperature protected from light. During this time, one drop of NucBlue was added to each well. Following incubation with dextrans and NucBlue, iPSNs were imaged using a Zeiss LSM 800 confocal microscope and a 40X objective. Nuclear intensity of fluorescent dextrans was determined with FIJI.

RNA FISH

Following one week of (G₄C₂)_n repeat RNA overexpression, iPSNs were rinsed briefly in 1X PBS and fixed in 4% paraformaldehyde in 1X PBS for 15 minutes at room temperature. iPSNs were then rinsed 3X 5 mins with 1X PBS, permeabilized with 1X PBS containing 0.3% Triton X-100 for 15 mins at room temperature, and subsequently washed 3X 5 mins with 1X PBS. iPSNs were then equilibrated in 1X SSC for 10 mins at room temperature. For RNase A treatment, 40 μ g/mL RNase A (Thermo Fisher Scientific) in 1X SSC was added to corresponding wells and iPSNs were incubated at 37°C for 45 mins. RNase treated iPSNs were washed briefly 2X with 1X SSC and then equilibrated in 1X SSC for 10 mins at room temperature. iPSNs were then equilibrated in 50% formamide in 2X SSC for 10 mins at 60°C and then hybridized with hybridization buffer (40% formamide, 2 mg/mL heat shock inactivated BSA (Sigma Aldrich), 1 mM ribonucleoside-vanadyl complex (New England BioLabs), 10 mM NaPO₄, 1X SSC) and probe mixture (10 μ g salmon sperm DNA (Thermo Fisher Scientific), 10 μ g E.coli tRNA (Millipore), 80% formamide, 0.2 μ M custom LNA probe) for 1 hour at 60°C. Custom 5' DIG labeled LNA probes (QIAGEN) are as follows: G₄C₂ probe: CCCCGGGCCCCGGCCCC lot number 302094012, scrambled probe: GTGTAACACGTCTATACGCCCA lot number 302495047. iPSNs were then washed 1X 20 mins with 50% formamide in 2X SSC at 65°C, 1X 15 mins with fresh 50% formamide in 2X SSC at 65°C, 1X 10 mins with 1X SSC in 40% formamide at 60°C, 3X briefly with 1X SSC at room temperature, 2X 5 mins with 1X SSC at room temperature, 1X 5 mins with TBS (50 mM Tris pH 7.5, 15 mM NaCl), 1X 5 mins with Tris Glycine (0.75% glycine, 0.2 M Tris pH 7.5), post-fixed with 3% paraformaldehyde in 1X PBS, and briefly rinsed 3X with 1X PBS. iPSNs were blocked with 1% normal goat serum and 5% heat shock inactivated BSA in TBS for 1 hour at room temperature and then incubated in 1:500 Mouse Anti-DIG (Jackson Immunoresearch) diluted in immunofluorescence buffer (2% heat shock inactivated BSA, TBS) overnight at 4°C. iPSNs were then washed 3X 5 mins with immunofluorescence buffer at room temperature and incubated with secondary antibody (1:500 Goat Anti-Mouse Alexa 568) diluted in immunofluorescence buffer for 30 mins at room temperature before undergoing a series of washes: 1X 5 mins TBS, 1X 5 mins Tris Glycine, 1X 5 mins PBS MgCl₂ (2 mM MgCl₂, 1X PBS), 1X 5 mins PBS, 1X 5 mins PBS with 1:1000 Hoescht, 1X 5 mins PBS. iPSNs were mounted with prolong gold antifade reagent with DAPI and imaged using a Zeiss LSM 800 confocal microscope and 63X objective. All solutions were made using RNase free water.

Evaluation of POM121 in Astroglia, Oligodendroglia, and HEK293T Cells

iPSC derived astrocytes were generated as previously described (Zhang et al., 2015). Primary human astrocytes (ScienCell) were cultured according to manufacturer instructions. HEK293T cells were obtained from ATCC and maintained in DMEM containing Pen/Strep and 10% FBS. Primary human astrocytes were nucleofected with G₄C₂ repeat RNA only constructs as described above. For overexpression of G₄C₂ repeat RNA only constructs in HEK293T cells, Lipofectamine 3000 (Thermo Fisher Scientific) was used according to manufacturer protocol. Nuclei from all cell types were isolated using the Nuclei PURE Prep Nuclei Isolation Kit (Sigma Aldrich) and imaged by SIM as described above. Postmortem oligodendrocyte nuclei were isolated from postmortem motor cortex and selected on the basis of Olig2 positive immunoreactivity.

QUANTIFICATION AND STATISTICAL ANALYSIS

All data analysis was conducted with Imaris version 8.3.1 or FIJI as described in individual experimental sections above. Analysis was either completely automated or blinded to eliminate bias. All statistical analyses were performed using GraphPad Prism version 7 and 8 (GraphPad). Statistical analyses were performed with regards to individual iPSC lines or patients such that the average of all nuclei or cells evaluated per iPSC line or patient represents N = 1 with total N per experiment and group as indicated in figure legends. Student's t test, One-way ANOVA with Tukey's multiple comparison test, or Two-way ANOVA with Tukey's multiple comparison test was used as described in figure legends. * p < 0.05, ** p < 0.005, *** p < 0.0005, **** p < 0.0001. Violin plots are used to display the full spread and variability of large datasets (> 10 data points). As opposed to bar graphs with individual data points representing the average value for each iPSC line analyzed (e.g., the exact graphical representation of our statistical analyses described above), violin plots were chosen to provide full transparency with regard to the true variability of each individual nucleus/cell. Center dotted line indicates median value. Two additional dotted lines indicate the the 25th and 75th percentiles. For smaller datasets, bar graphs displaying individual data points shown where error bars represent ± SEM